This document is confidential and is proprietary to the American Chemical Society and its authors. Do not copy or disclose without written permission. If you have received this item in error, notify the sender and delete all copies.

Molecular and Structural Characterization of Isomeric Compounds in Atmospheric Organic Aerosol Using Ion Mobility – Mass Spectrometry

Journal:	The Journal of Physical Chemistry
Manuscript ID	jp-2022-06459k.R1
Manuscript Type:	Article
Date Submitted by the Author:	09-Dec-2022
Complete List of Authors:	West, Christopher P; Purdue University, Chemistry Mesa Sanchez, Daniela; Purdue University System, Chemistry Morales, Ana; Purdue University, Chemistry Hsu, Yun-Jung; Purdue University, Chemistry Ryan, Jackson; Purdue University, Chemistry Darmody, Andrew; Purdue University, Slipchenko, Lyudmila; Purdue University, Chemistry; Laskin, Julia; Purdue University, Department of Chemistry Laskin, Alexander; Purdue University, Chemistry

SCHOLARONE™ Manuscripts

Molecular and Structural Characterization of Isomeric Compounds in Atmospheric Organic Aerosol Using Ion Mobility – Mass Spectrometry

Christopher P. West¹, Daniela Mesa Sanchez¹, Ana C. Morales¹, Yun-Jung Hsu¹, Jackson Ryan¹, Andrew Darmody^{1,2}, Lyudmila V. Slipchenko, Julia Laskin¹, Alexander Laskin^{1,3*}

¹Department of Chemistry, Purdue University, West Lafayette, IN, USA

²Department of Aeronautics and Aerospace Engineering, Purdue University, West Lafayette, IN

³Department of Earth, Atmospheric & Planetary Sciences, Purdue University, West Lafayette, IN, USA

Correspondence to: Alexander Laskin (alaskin@purdue.edu)

Manuscript Submitted to:

Journal of Physical Chemistry A

Special Issue "Advances in Atmospheric Chemical and Physical Processes"

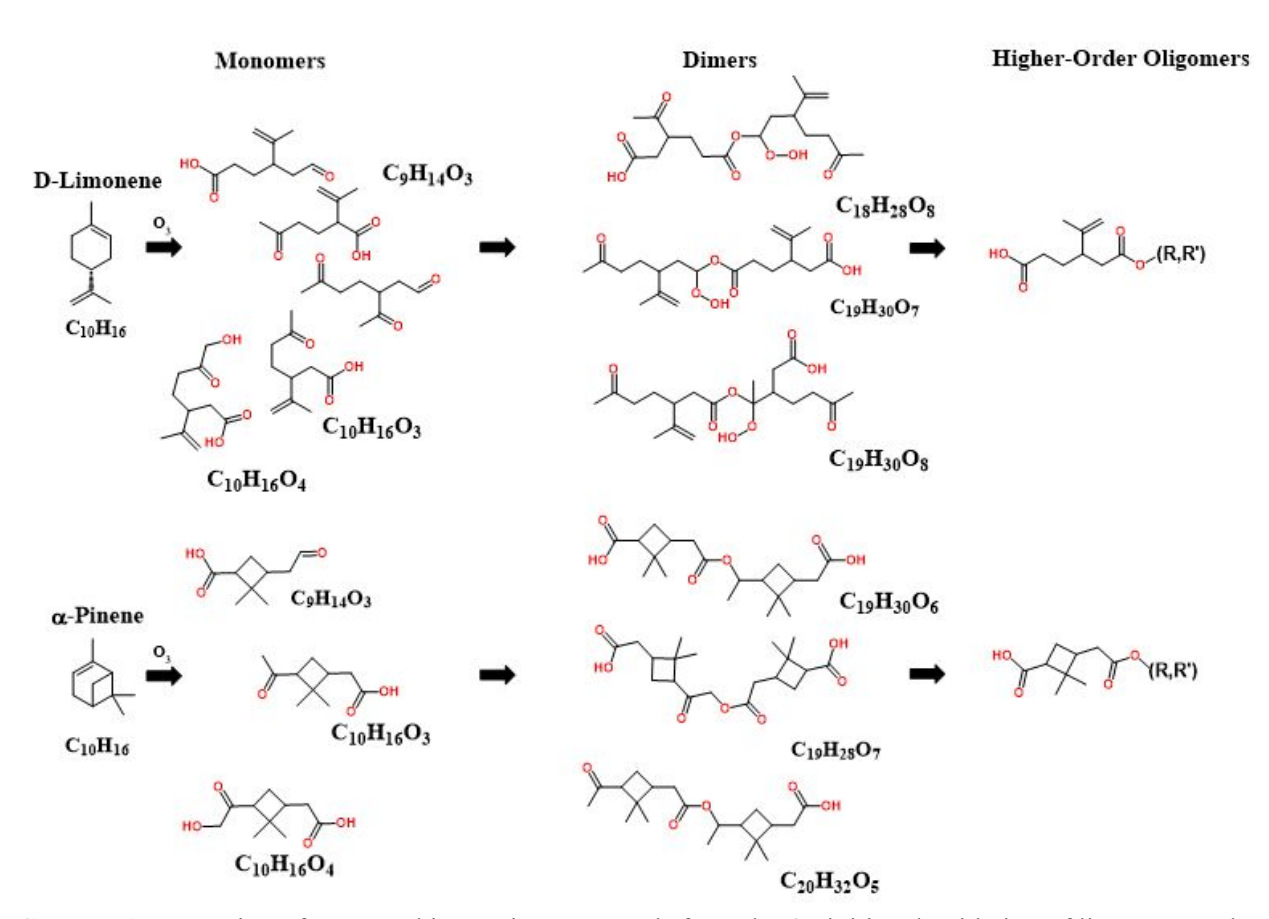
December 9, 2022

Abstract. Secondary organic aerosol (SOA) formed through multi-phase atmospheric chemistry makes up a large fraction of airborne particles. The chemical composition and molecular structures of SOA constituents vary between different emission sources and aging processes in the atmosphere, which complicates their identification. In this work, we employ drift tube ion mobility spectrometry with quadrupole time-of-flight mass spectrometry (IM-MS) detection for rapid gasphase separation and multi-dimensional characterization of isomers in two biogenic SOA produced from ozonolysis of isomeric monoterpenes, D-limonene (LSOA) and α-pinene (PSOA). SOA samples were ionized using electrospray ionization (ESI) and characterized using IM-MS in both positive and negative ionization modes. The IM-derived collision cross-sections in nitrogen gas (DTCCS_{N2}) for individual SOA components were obtained using multi-field and single-field measurements. Novel application of IM multiplexing/high-resolution demultiplexing methodology was employed to increase sensitivity, improve peak shapes, and augment mobility baseline resolution, which revealed several isomeric structures for the measured ions. For LSOA and PSOA samples, we report significant structural differences of the isomer structures. Molecular structure calculations using density functional theory combined with theoretical modeling of CCS values provide insights into the structural differences between LSOA and PSOA constituents. The average DTCCS_{N2} values for monomeric SOA components observed as [M+Na]⁺ ions are 3 – 6% higher than those of their [M-H]- counterparts. Meanwhile, dimeric and trimeric isomer components in both samples showed an inverse trend with the relevant values of [M-H]- ions being 3 - 7% higher than their [M+Na]⁺ counterparts, respectively. The results indicate that the structures of Na⁺-coordinated oligomeric ions are more compact than those of the corresponding deprotonated species. The coordination with Na⁺ occurs on the oxygen atoms of the carbonyl groups leading to compact configuration. Meanwhile, deprotonated molecules have higher DTCCS_{N2} values due to their elongated structures in the gas-phase. Therefore, DTCCS_{N2} values of isomers in SOA mixtures depend strongly on the mode of ionization in ESI. Additionally, PSOA monomers and dimers exhibit larger DTCCS_{N2} values (1-4%) than their LSOA counterparts owing to more rigid structures. The presence of a cyclobutane ring with functional groups pointing in opposite directions in PSOA compounds, as compared to non-cyclic flexible LSOA structures, forming more compact ions in the gas phase. Last, we investigated effects of direct photolysis on the chemical transformations of selected individual PSOA components. We use IM-MS to reveal structural changes associated with aerosol aging by photolysis. This study illustrates detailed molecular and structural descriptors for the detection and annotation of structural isomers in complex SOA mixtures.

Introduction

Secondary organic aerosol (SOA) formed through multi-phase atmospheric chemistry makes up a significant fraction of airborne particulate matter in the atmosphere. $^{1-4}$ The emissions of biogenic volatile organic compounds (BVOCs) represent the largest flux of all non-methane gas-phase compounds into the atmosphere, where $\sim\!60\%$ of the total BVOC budget is attributed to isoprene and the monoterpenes. $^{5-7}$ BVOCs react with atmospheric oxidants, such as ozone (O₃), nitrogen oxides (NO_x) and radicals (i.e., \cdot OH, \cdot NO₃), to form low-volatility highly oxygenated organic compounds, which promote nucleation and growth of SOA. $^{1,8-10}$ Monoterpenes represent a large group of $C_{10}H_{16}$ structural isomers and enantiomers emitted from different sources. Monoterpenes exhibit different reaction pathways and kinetics for oxidation and SOA formation based on the location and number of double bonds in their structures. This immense complexity of SOA and the presence of numerous isomeric structures complicate its analytical characterization 11,12 and limit our understanding of the aerosol physical properties such as viscosity, refractive indexes, and volatility. $^{13-16}$

The ozonolysis of two $C_{10}H_{16}$ monoterpene isomers: α -pinene (PSOA) and limonene (LSOA) have been used in the past to elucidate the effects of the chemical structures of BVOC precursors and their corresponding products on the chemical aging and evolution of the physical properties of SOA. $^{17-25}$ The ozonolysis of α -pinene and limonene have been reported to form numerous isomeric monomers and oligomers (dimers, trimers, and tetramers). 26,27 Scheme I illustrates the formation of structural isomeric compounds from the O_3 -initiated oxidation of limonene and α -pinene to yield several monomeric, dimeric, and higher-order oligomeric structures differing by the number of oxidized monomer (R, R') units. The molecular structures of LSOA and PSOA exhibit unique products characteristic of the initial BVOC structures. Specifically, PSOA products contain a four-membered cyclobutane ring, while LSOA products are open-chained structures. Understanding the formation pathways of SOA and their chemical reactivities are important for predictions of aerosol properties. Therefore, case studies detailing systematic differences between SOA mixtures from different BVOC sources and oxidants require advanced multidimensional analytical methods to deconvolute and predict molecular- and often isomer-specific mechanisms and rates of SOA formation and ageing.



Scheme 1. Formation of structural isomeric compounds from the O₃-initiated oxidation of limonene and α-pinene monoterpenes $(C_{10}H_{16})$ to yield monomers, dimers, ^{17,28,29} and higher-order oligomer structures that differ by number of oxidized monomer units, denoted as R, R'. Selected dimers of LSOA potentially form from the monomer-Criegee reactions proposed by Hammes et al. (2019). ¹⁷ Selected dimers of PSOA form by dimerization reactions determined and reported by Yasmeen et al. (2010, 2012), ^{30,31} Kahnt et al. (2018), ³² and Kenseth et al. (2018, 2020), ^{28,29}

Despite the structural differences between the molecular structures of LSOA and PSOA, their mass spectra are quite similar. 11,17,26,27,33–39 The elemental composition of the SOA components have been extensively studied and thousands of individual species have been assigned based on accurate mass measurements provided by high-resolution mass spectrometry (HRMS). 40 However, isomer-specific structural characterization in SOA samples requires additional analytical methods, such as separation or tandem mass spectrometry (MSn) analyses. 12,32 Liquid chromatography (LC) and gas chromatography have been routinely employed for the separation of complex constituents in lab-generated biogenic SOA, 28,41–46 combustion related primary OA 47,48 and field-collected OA samples. 49–54 However, long LC gradients, the presence of co-eluting analyte peaks, and limited analytical standards present a challenge for SOA characterization using LC-MS. Incorporation of MSn workflows for isomer differentiation has been employed for their structural characterization. For example, the analysis of atmospherically relevant SOA in previous studies 32,55,56 resulted in the extensive characterization of esters, peroxides, and organosulfates along with several dimeric organic compounds in PSOA 32 and LSOA. 56 Tandem MS experiments 55

revealed characteristic fragmentation of several compound classes in SOA samples. However, structural characterization of SOA components using MSⁿ usually requires a comparison with synthesized standards or reference spectra, which are limited for SOA compounds. Modern ion mobility mass spectrometry (IM-MS) measurements overcome some of the limitations of LC-MS and enable high throughput characterization and experimentally informed annotation of isomeric components in complex organic mixtures such as SOA.^{26,57}

IM-MS is a powerful post-ionization separation technique that separates gas-phase ions based on their mobility through an inert buffer gas such as N2.58,59 Ions are pulsed into the low electric field drift tube and separated in a few milliseconds in the gas phase based on their collision cross-sections, mass-to-charge ratio (m/z), and charge states. ⁵⁸⁻⁶¹ Analyte identification in this measurement is aided by converting the ion-specific drift time values, t_D , into the collision crosssection (CCS) using the Mason-Schamp equation. 61-63 Ion mobility measurements provide an additional level of fingerprinting for SOA components using the CCS as a structural descriptor and enable gas phase separation of isomers in complex mixtures. 63,64 In certain cases, measured CCS offers molecular description of the gas-phase three-dimensional (3D) configuration of ions formed in ionization, 59,65 which has been used for studying the folding and unfolding of protein complexes^{66–72} and structures of DNA molecules.^{73,74} The mobility of ions in IM-MS is affected by the charging effects in electrospray ionization (ESI), which often generates several ionized states of analyte molecules⁷⁵ such as protonated and deprotonated species along with cation or anion adducts. The mode of ionization influences the conformation and selectivity of ionized analytes. IM-MS is an effective method for the structural characterization of SOA constituents, which complements the capabilities of tandem mass spectrometry^{32,76} and IR spectroscopy.^{77–80} Recently, IM-MS was employed for the identification, structural characterization, and rapid separation of isomeric components in complex SOA mixtures.^{26,57}

Early IM-MS studies^{57,75,81} of gas-phase and aerosol constituents have demonstrated its potential for studying mechanisms of atmospheric aerosol chemistry. Specifically, IM-MS has been used to separate and identify selected α-pinene oxidation products and ambient aerosol constituents based on their gas phase mobilities.⁵⁷ Other studies^{82,83} reported measured versus modelled CCS values of relevant atmospheric organic compounds and developed two-dimensional CCS – *m/z* trendlines for the assessment of structure-class relationships. Travelling wave IM-MS has been used to measure the CCS values of two dimer ester products of PSOA.⁷⁵ Meanwhile, a differential mobility analyzer has been used to measure CCS and ion mobility of few monomeric isomers of PSOA.⁸⁴ Although the initial works^{26,57,82–86} reported on the use of IM-MS for SOA characterization, a comprehensive, untargeted characterization of structural isomers in biogenic SOA has not been reported. Drift tube IM-MS instruments are ideally suited for the accurate determination of CCS values of compounds (DTCCS) in complex mixtures.^{59,87} The development of DTCCS library databases for atmospheric SOA systems will facilitate rapid and accurate isomer

detection, which in turn will aid in predictive understanding of their chemical and physical properties.

In this work, we present a systematic chemical characterization study of laboratory generated PSOA and LSOA mixtures using a drift tube ion mobility quadrupole time-of-flight mass spectrometer.⁴⁸ Accurate measurements of ^{DT}CCS values using stepped-field IM-MS allowed us to construct a ^{DT}CCS library of the analyte ions in both mixtures. We examine structural differences between PSOA and LSOA based on the experimentally determined ^{DT}CCS versus *m/z* trends and theoretical calculations.⁴⁷ Additional temporal multiplexing experiments⁸⁸ were performed to increase the sensitivity and resolution of IM measurements. The latter is achieved using high resolution demultiplexing of the experimental data.^{58,89} We present the first application of the IM multiplexing/high resolution demultiplexing approach for the characterization of overlapping isomers in SOA that were not resolved in conventional IM-MS measurements. Last, we investigated the effect of direct photolysis on the chemical transformations of individual PSOA components to assess structural changes associated with aerosol aging.

Experimental Methodology

Generation and Aging of SOA samples

PSOA and LSOA were generated through ozone-initiated oxidation of limonene (98% purity; CAS: 5989-27-5, Sigma Aldrich Inc.) and α -pinene (98% purity; CAS: 7785-70-8, Sigma-Aldrich Inc.) injected into a custom 200 L Teflon sealed bag equipped with two gas inlets, one exhaust port, and one sample injection port. Approximately 130 L of ultrapure nitrogen gas (N₂; 99.99% purity, Indiana Oxygen) were initially flowed into the bag at a flow rate of 10 slpm using mass flow controller (TSI Inc.). Purified oxygen (O₂; 99.99% purity, Indiana Oxygen) was flowed through an ozone (O₃) generator (model OG-2; UVP Inc.) equipped with 185 nm UV lamp and 2B ozone monitor (Thermo Scientific Inc, Waltham, MA). The flow of photogenerated ozone was then directed inside the Teflon bag to reach a final measured mixing ratio of \sim 2 ppm O₃. No seed aerosols were used for SOA generation experiments. The SOA were generated with relatively high mass loadings to generate enough sample for molecular characterization following the procedures by Walser et al.²⁷

The limonene and α -pinene were diluted (75:25 % v/v) in LCMS grade cyclohexane (> 99.99 % purity, Sigma Aldrich Inc.) and obtained mixtures were used for injection. Cyclohexane was incorporated in the reagent solutions to scavenge OH radicals and prevent unintended OH radical oxidation.²⁷ To maintain an approximate 1/1 molar ratio of BVOC to O₃, $\sim 2.46~\mu$ L BVOC/cyclohexane mixture was injected using a 10 μ L Hamilton syringe, which resulted in a 2:2 ppm BVOC/O₃ mixing ratio. The BVOC and ozone mixture was allowed to react for \sim 25 – 30 min in the Teflon bag until *high* mass concentration of SOA was formed. The particle size and mass

concentrations were monitored online with a scanning mobility particle sizer (SMPS, TSI Inc., model 3062) equipped with a differential mobility analyzer (DMA, TSI Inc., model 3081) and a condensation particle counter (CPC, TSI Inc., model 3776). SOA particles were collected on 1.0 um pore size polytetrafluoroethylene (PTFE) membrane filters (OmniporeTM) using vacuum pulled filtration of aerosols and stored at -20 °C prior to analyses. To simplify sample preparation and interpretation of the IM-MS datasets, no seed aerosol was used and effects of the wall losses on the SOA composition were assumed to be similar between LSOA and PSOA experiments. Additional details of the SOA generation experiments, the particle size distributions and corresponding mass loadings are described in Supplementary Note 1 and Figures S1 – S2 of the SI file. A quarter of each PTFE filter with collected sample was cut and extracted into 10 mL of acetonitrile (Optima, Sigma-Aldrich Inc.) followed by ultrasonication for 20 min and vortexing for 30 sec at 2500 rotations min⁻¹. Obtained extracts were filtered using 0.20 um PTFE syringe filter cartridges (Thermo Inc.). The PTFE cartridges were prewetted before analyte filtration using fresh solvent to minimize adsorption of the analyte on the filter substrate. The SOA extracts were further diluted to a mass concentration of $\sim 6 \mu g \text{ mL}^{-1}$ and reconstituted in a 70/30 (v/v %) LCMS grade acetonitrile (ACN)/water (H₂O) (Optima, Fisher Scientific Inc.) solvent. The SOA extracts were prepared fresh and subsequently analyzed, in order to minimize effects of hydrolysis and side reactions occurring in the mixtures after addition of water.

Aqueous extracts of PSOA in 70/30 ACN/H₂O (v/v %) solution were irradiated in a custom-built photoreactor that emits UV-LED light at ~ 310 nm. The 310 nm light represents tropospheric UV radiation occurring below the ozone layer. The narrow band LED light was used instead of solar simulator to allow simplified quantitation of the experimental photochemistry calculations summarized in Supplemental Note 2 of the SI file. The sample was left to photolyze for 60 min and aliquots were collected at varying time intervals during the photolysis. The temperature of the photoreactor was monitored during photolysis and did not exceed room temperature (~24 °C). The photon flux of the photoreactor device (F_{LED}) was measured using the azobenzene chemical actinometer system by preparing a 0.05 mM azobenzene solution in ethanol in the presence of 1 mM potassium hydroxide (Honeywell Inc.). The experimental F_{LED} was measured to be ~ 1.26 x 10¹⁶ photons cm⁻² s⁻¹. Additional details of the photoreactor and flux calculations are described in Supplementary Note 2 and Figure S3 of the SI file.

Ion Mobility-Mass Spectrometry (IM-MS) Analysis

PSOA and LSOA extracts were infused into a 6560 ion mobility quadrupole time-of-flight (IM Q-TOF) mass spectrometer (Agilent Technologies, Santa Clara, CA). All analytes were ionized via electrospray ionization using a commercial dual jet stream source. Samples were placed into a 500 μ L Hamilton syringe and introduced at a flow rate of 5 μ L min⁻¹ using a syringe pump (Legato 180 syringe pump, KD Scientific, Holliston, MA). The following source parameters were used for ESI: high voltage of 2000 V nozzle voltage, and V_{Cap} voltage set to 4000 V,

nebulizing gas flow of 7 L min⁻¹, \sim 300 °C drift gas, and 200 °C sheath gas temperature. After the MS inlet, the ions are focused by the high pressure ion funnel and accumulated into the lower pressure trapping ion funnel. The ions are then pulsed into the N_2 filled drift tube (3.9 \pm 2.0 Torr) under the influence of an applied electric field and are subsequently separated according to their drift time in inert N_2 gas. The maximum drift time in these experiments was set to 70 ms with a 40 ms ion funnel trap time and 0.2 ms release time. The instrument was operated in both positive and negative ion polarities. The TOF was operated in the "low" mass range mode (m/z 50-1700) using a "high sensitivity" TOF slicer, a 2 GHz digitizer, and mass resolution of 15,000. CCS values were measured using the stepped-field method. Multiplexing IM experiments were conducted in the 4-bit mode, where the ion accumulation and release times were set to 3 ms and 0.2 ms, respectively. Therefore, multiplexed IM experiments resulted in 8 discrete ion pulses over the 70 ms drift time range. A worklist in the Agilent MassHunter acquisition software consisting of multifield and 4-bit multiplexing methods were used to automate the IM-MS data acquisition. Additional IM Q-TOF experimental parameters are provided in Supplementary Note 3 of the SI file.

Additionally, direct infusion high-resolution mass spectrometry (HRMS) measurements were performed using the Q-ExactiveTM HF-X Orbitrap interfaced with heated electrospray ionization probe (HESI) and IonMAX housing (all from Thermo Scientific Inc.). The following conditions were used for the HESI source operation; 80 °C probe heater temperature, 250°C inlet capillary temperature, 13 units of sheath gas flow, 3 units of auxiliary gas flow, 1 unit of sweep gas flow, 3.5 kV spray potential, and 80 RF S-lens level. The instrument was operated at m/Δm 240,000 resolving power at 200 *m/z* and acquisition rate of 1.5 Hz in the full MS scan mode (100 – 1200 *m/z* range). Additional details of HRMS experiments and data analysis are described in Supplementary Note 4 of the SI file. In source collision induced dissociation (CID) experiments where conducted by applying accelerating voltage in a range of 0 – 60 eV in increments of 10 eV to distinguish between covalently bonded dimer and trimer ions characteristic of SOA components from ion-molecule monomer adducts that may form in the ion source.³⁹Additional effects of concentration on the MS response were also studied. Results of these experiments are illustrated in Supplementary Note 5 and Figures S4 – S5 of the SI file.

All molecules in the SOA samples were preferentially observed as [M+Na]⁺ species in (+)ESI mode, while [M-H]⁻ ions were detected in (-)ESI. Occasionally, protonated molecules, [M+H]⁺, were also observed. Formula assignments in the Q-TOF and HRMS datasets were performed based on high order mass defect analysis⁹⁴ of the two-dimensional homologous series of MS peaks, which clusters peaks differing by the number of -CH₂, -H₂, and -O units.. The following constraints were applied for all formula assignments: C_{1-40} , H_{1-100} , O_{1-25} , N_{0-1} , mass tolerance of \pm 5.0 ppm for IM Q-TOF and \pm 2.0 ppm for HRMS datasets. Elemental formulas of representative species from each group were assigned using the MIDAS molecular formula calculator (v 1.1; http://nationalmaglab.org/user-facilities/icr/icr-software). All other peaks in each

group were subsequently assigned using the known number of -CH₂, -H₂, and -O units that distinguish them from the representative species.

IM-MS Data Processing, Analysis, & CCS Calculations

 $^{\mathrm{DT}}\mathrm{CCS}_{\mathrm{N2}}$ values for prominent isomer components in PSOA and LSOA were calculated using the IM-MS Browser software (Agilent, Santa Clara, CA) using the stepped-field CCS calculation method. 59,93,95 The stepped-field method yields accurate and reproducible determination of the analyte ion's CCS value. 93 The instrumental relative standard deviation for the calculated CCS values of this method is estimated to be within \pm 0.29% for inter-laboratory comparison. 93 For multi-field CCS calculation, the software determines t_0 of the ion, which is the post drift tube flight time of the ion and uses this value to accurately calculate time the ions spend in the drift tube (t_D). This is performed in the IM Browser software by constructing a plot of the observed drift times of the measured ion at various drift field strengths (850–1450 V) followed by a linear fit of the datapoints over the seven field measurements to determine the y-intercept, t_0 . 59,96 Supplementary Note 6 and Figure S6 of the SI file provide an example of this calculation. After the y-intercept is determined, the obtained t_0 values are then subtracted from the total flight to obtain the corrected t_D of the ion. The t_D term is then incorporated into the Mayson-Schamp equation 62 (eqn. 1) to compute the CCS of the corresponding ion:

$$DTCCS_{N2}(\Omega; Å^{2}) = \frac{(18\pi)^{1/2}}{16} \frac{ze}{(k_{B}T)^{1/2}} \frac{3}{16} \sqrt{\left[\frac{1}{m_{l}} + \frac{1}{m_{B}}\right]} \frac{t_{D}E}{L} \frac{p_{0}}{p} \frac{T}{T_{0}} \frac{1}{N_{0}}$$
(1)

In this expression, L is the drift tube length, m_I is the mass of the analyte ion, m_B is the mass of the buffer gas molecule, E is the electric field strength, k_B is the Boltzmann constant, z is the absolute ion charge (nominal), e is the elementary charge of the electron, p and T are the experimental pressure and temperature of the reagent gas in the drift tube, p_0 and T_0 are the standard pressure and temperature at 760 Torr and 273.15 K, N_0 is the number gas density of the reagent gas at T_0 , and T_0 0.

Datasets from IM multiplexing experiments were initially demultiplexed and interpolated using the PNNL PreProcessor 3.1 (2021.04.21) software (https://pnnl-comp-mass-spec.github.io/PNNL-PreProcessor). 97,98 A 1-to-3 drift bin interpolation, and 3 data point moving average smoothing function was used for demultiplexing. The resulting demultiplexed data was filtered through MassProfiler 10.01 (Agilent, Santa Clara, CA) to generate a feature list (infusion filtering, common organic molecule isotope model). This feature list, the raw multiplexed file, and the interpolated demultiplexed PNNL PreProcessor file output underwent additional processing via High Resolution Demultiplexer 2.0 (HRdm 2.0; G5294AA, Agilent, prerelease build 21).46

This software performs a refined demultiplexing, targeting specific features, and taking into account known artifacts of the transformation. This results in an increase of the mobility drift resolution at full width-half maximum (FWHM) from 50 to as high as 250 after HRdm processing at the highest processing setting.

For the multiplexed IM experiments and processed HRdm datafiles, we use the single-field CCS calculation⁹⁵ For this method, the CCS calibration was performed by linear regression of tune mix reference ions with known CCS at the exact same tuning parameters as described in Supplementary Note 3 of the SI file. The ion mobility feature extraction algorithm function in IM Browser software were used to detect IM–MS features and compute for the CCS of the ions.

Computational Chemistry and Ion Mobility Trajectory Calculations

Theoretical computational chemistry calculations were performed using Gaussian 16⁹⁹ software. The isomeric molecules of interest were constructed using GaussView (version 5.0.9). Density functional theory (DFT) at the ωB97XD/6-311+G (d,p) level of theory was utilized for obtaining energy minimized structures of ions in gas phase. Additional details of DFT computational calculations are discussed in Supplementary Note 7 of the SI file. Ion mobility trajectory computations were performed using the Ion Mobility Spectrometry Suite (IMoS; https://www.imospedia.com/imos/) GUI and software package (MATLAB Inc.). 100 The theoretical CCS_{N2} of the DFT optimized gas-phase ions were computed numerically using the trajectory method with a 4-6-12 Lennard-Jones (TMLJ) interaction potential and ion-induced dipole interaction. 101 The TMLJ method was used instead of classical projection area and hard-sphere core model approaches due to the higher accuracy exhibited by TMLJ method. 102 The polarizability and radius of the N₂ buffer gas was set to 1.7 Å² and 1.5 Å, respectively. The polarizability of the buffer gas describes the long-range ion induced dipole attractive interaction. ¹⁰³ Pressure and temperature were set to those of the experiment [3.92 Torr (522.6 Pa) and 298.5 K (25 °C)]. The number of N₂ gas molecules was to 3 x 10⁶ to converge to accurate program computations. 102 The LJ potentials were used from literature for C, H, and O main group elements, using the LJ parameters from Campuzano, Bush et al., 103 and MOBCAL 101 however Na+ LJ potentials may require further optimization.

Results & Discussion

Figure 1 illustrates the IM-MS data acquired for LSOA and PSOA. Figures 1a,b show characteristic mass spectra exhibiting ranges of monomeric, dimeric, and trimeric products, similar to previous studies. 11,26,27,35 The elemental composition of ions was determined based on HRMS measurements using the Q-Exactive instrument. These assignments were subsequently used to assign peaks observed in the Q-TOF data acquired with a lower mass resolution. Additional HRMS spectra of the assigned species and compositional information related to LSOA and PSOA mixtures are included in Figure S7 of the SI file. Both mixtures contain similar multi-functional

oxidized organic compounds as inferred from Kendrick mass defect (CH₂ and O) groupings and VanKrevelen maximum carbonyl ratio¹⁰⁴ diagrams shown in Figures S8 – S9, respectively. Two mixtures differ by their total number of assigned formulas as LSOA species are more ionizable than PSOA counterparts, leading to higher number of assignments in LSOA samples. Figures 1c,d illustrate the mobility separated ions of the LSOA and PSOA mixtures, measured in positive and negative modes, respectively. Figures 1e-h show characteristic two-dimensional (2D) heatmaps of IM drift time (ms) vs. *m/z* for LSOA and PSOA samples. The 2D heatmaps show the characteristic drift separated ions, their abundances, and analyte distributions across the 150-700 *m/z* range spanning monomers and oligomeric ions in the IM-MS experiments. All 2D heatmaps for LSOA and PSOA measured in (+/–)ESI-IM-MS measurements are shown in Figure S10. In the IM-MS experiments, we observe occasional 'streaking' across the 2D heatmap which results from fragmentation of larger multimer ions occurring after the drift tube and leaking/overfilled ions in the trapping funnel of IM-Q-TOF. Those ions were excluded from the analysis.

In line with similar CID experiments reported previously to test intermolecular bond strength in the α -pinene dimers, 57 our results shown in Figure S4 indicate that the observed multimer ions do not fragment at <25eV voltages, suggesting that their monomer units are covalently bound. Additionally, oligomerization reactions may accelerate in the ESI microdroplets, which would result in their higher abundance in the analyzed mixtures. $^{105-107}$ To test this effect, we analyzed SOA mixtures infused into HRMS at different extract concentrations ranging from 0.5 to 6 μg mL-1, and quantified relative intensities of multimers to monomers as a function of concentration. Because all oligomerization steps are bimolecular reactions, higher extract concentrations would lead to larger fractions of the detected multimers if acceleration chemistry in microdroplets occurred. Our results shown in Figure S5 indicate that dimer formation might be accelerated only by ~ 20 % using the analyte concentrations employed in our study. Further results of these tests are summarized in Supplementary Note 5 of the SI file."

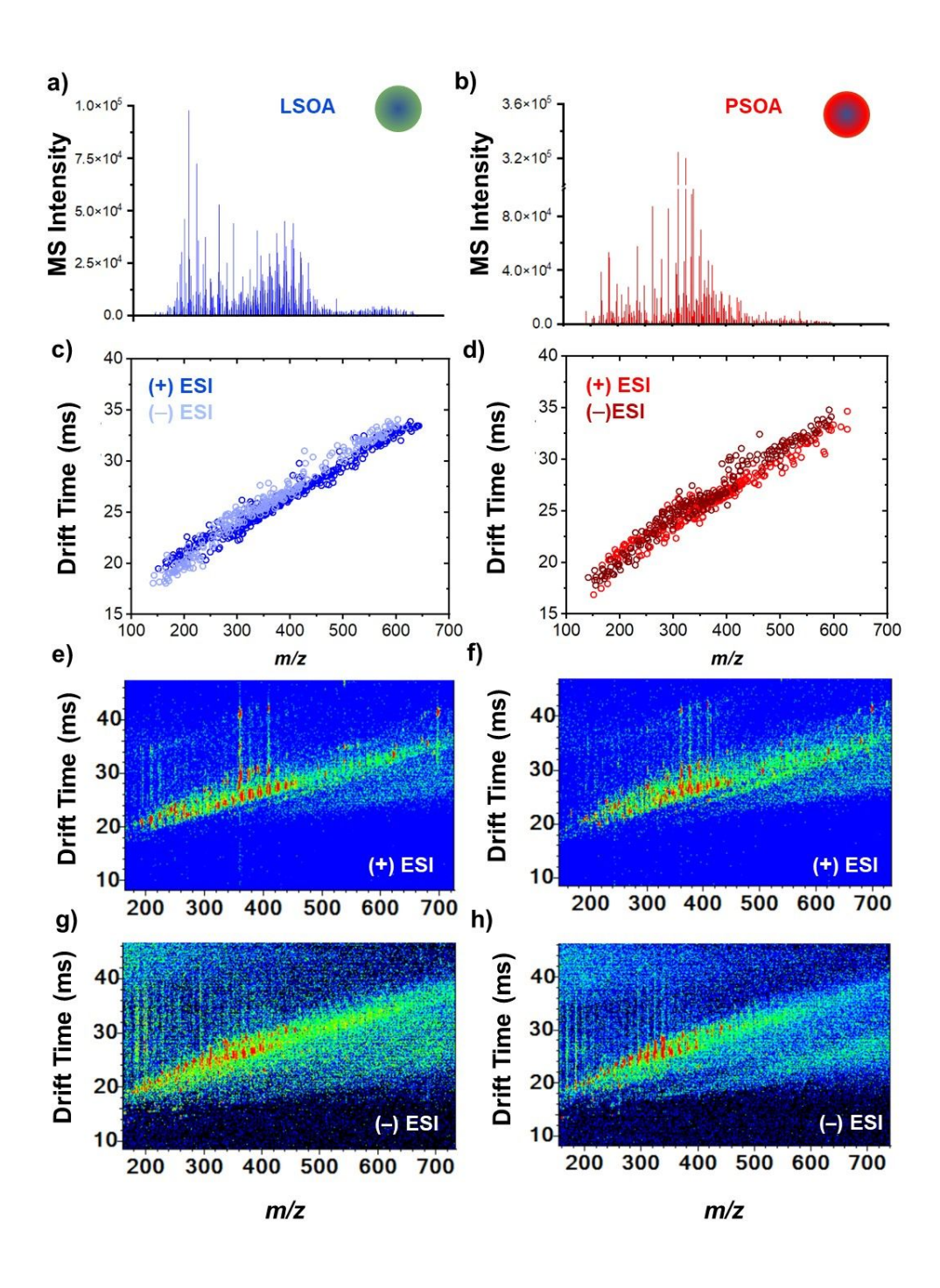


Figure 1. Q-TOF mass spectra acquired for a) LSOA (blue) and b) PSOA (red) samples. The drift time separated IM-Q-TOF features identified for c) LSOA and d) PSOA samples in (+/–)ESI modes. The colors in c) and d) plots correspond to the mode of polarity, blue/light blue for LSOA and red/maroon color for PSOA, respectively. Two-dimensional IM drift time (ms) vs experimental *m/z* heatmaps for e) (+)ESI and f) (–)ESI modes for PSOA representative sample.

As expected, the drift time increases with an increase in the m/z of the ion. The drift times of monomeric ions are higher in positive mode than in negative mode. Whereas the drift times for the dimer and trimer ions measured in negative mode appear to be slightly larger than those of their cationic counterparts. The apparent drift times shown here are experimental values which vary for different IM-MS instruments and are therefore not molecular-specific metrics. The intrinsic properties of ions that underline their mobility – structure relationships are the CCS values, which are independent of the instrument and serve as reproducible structural descriptors of the analytes in complex SOA samples.

Figure 2 presents a summary of the measured $^{DT}CCS_{N2}$ values for LSOA and PSOA analyte ions computed using eq. 1 versus their m/z values. The results are shown as scatter plots projected onto the 2D CCS versus m/z plane^{59,83} used to determine the structure-class relationships for the measured analytes. They represent the molecular ordering of organic compounds based on the mass and size of the ions separated by monomer, dimer, and trimer classification. Figures 2a-d show results for LSOA and PSOA analytes detected in positive and negative ionization modes. In order to place these results into the context of known SOA components, we highlight regions characteristic of organic molecules with moderately low O/C ratios of 0.3 – 0.6 indicative of the mono-carboxylic groups ($dark\ gray$ shading) and those with O/C ratios of 0.2 – 0.4 typical for molecules with alcohol and ester moieties ($light\ gray$ shading).⁸³

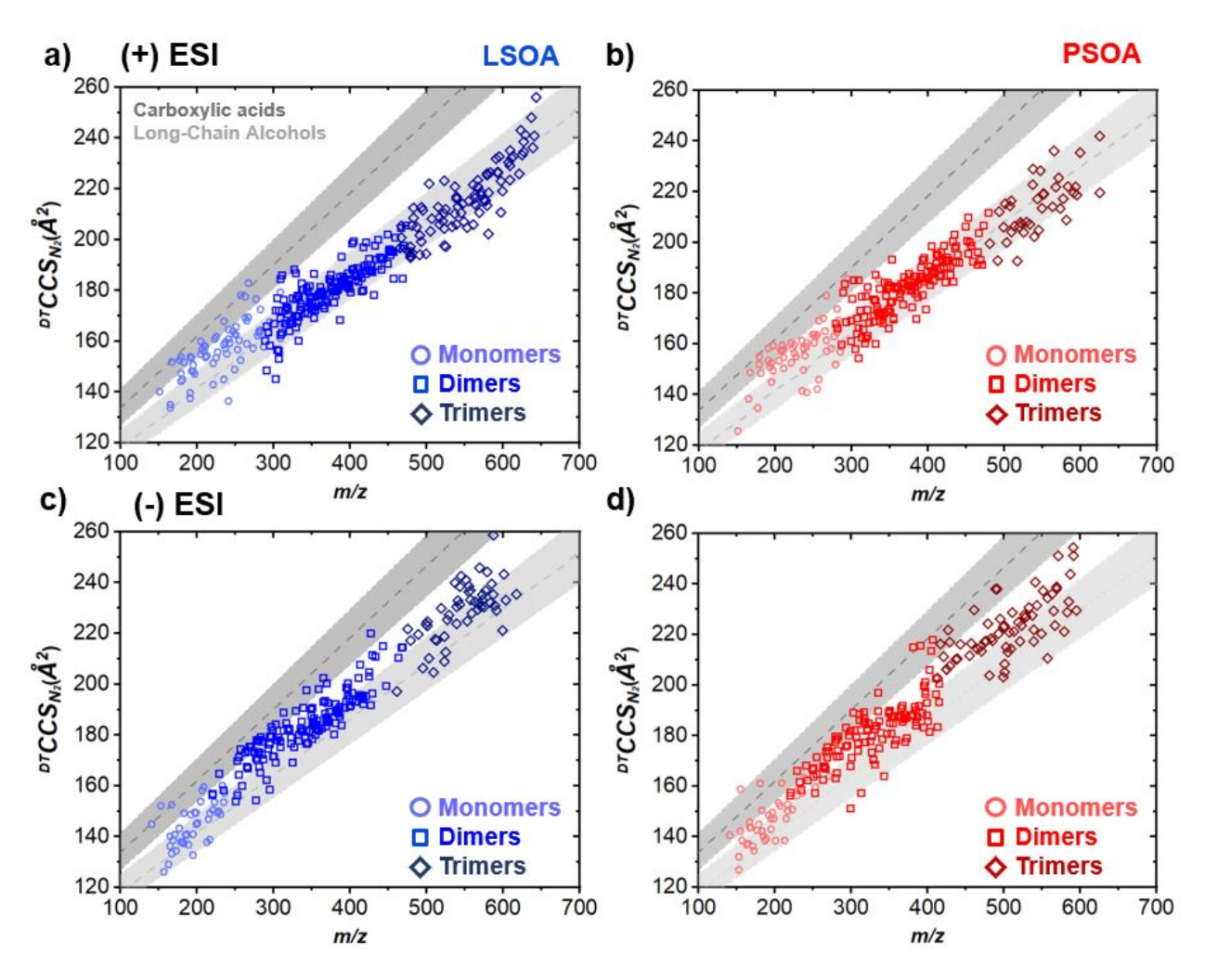


Figure 2. Collision cross-sections ($^{DT}CCS_{N2}$) vs m/z for the ions measured in (+)ESI and (-)ESI modes for LSOA and PSOA mixtures projected along the 2D $^{DT}CCS_{N2} - m/z$ plane. Trendlines and their uncertainties define the shaded trend regions (reported as upper and lower limits) for carboxylic acids (dark gray reference area) and long-chain alcohols (light gray reference area) reported previously. ⁸³ a) and b) represent (+)ESI CCS data for LSOA and PSOA grouped by fractions of monomers, dimers, and trimer ion structures. c) and d) represent measured (-)ESI mode CCS data for LSOA and PSOA ions.

We report a $^{DT}CCS_{N2}$ library of SOA compounds that total 1,085 $^{DT}CCS_{N2}$ across both SOA samples measured in both positive and negative modes for 324 (LSOA) and 256 (PSOA) constituents observed as [M+Na]⁺ ions along with 266 (LSOA) and 239 (PSOA) compounds observed as deprotonated [M–H]⁻ molecules. The CCS values range from $\sim 120-265$ Ų in size over the 140 -650 m/z range. The observed trends in the $^{DT}CCS_{N2}$ versus m/z plots and a quantitative assessment of the $^{DT}CCS_{N2}$ values are used to infer structural differences between the components of LSOA and PSOA mixtures. Figures 2a,b show that monomer ions measured in positive mode for both mixtures are localized within the carboxylic acids reference region but are systematically 2-5% below the center trendline. It has been reported that monomers in both SOA mixtures have characteristic O/C ratios^{27,108} of 0.4-0.8 and typically contain one or two

carboxylic acid moieties, 27 which is consistent with the observed trend in their CCS values. Some monomers may also contain one or more carbonyl functional groups (i.e., ketones, aldehydes) resulting in smaller CCS values that are outside of the carboxylic acids reference area. The PSOA monomer ions observed in positive mode have slightly larger (1.2 – 2%) CCS values compared to those of LSOA, which is consistent with more rigid structures of PSOA components containing a cyclobutane ring. On the other hand, the CCS values of oligomeric (dimers and trimers) ions match well the alcohols reference region, consistent with the less oxygenated oligomeric molecules with lower O/C ratios of ~ 0.3 . Oligomeric products of SOA are formed through esterification and aldol condensation reactions, 32,109 which produce a water molecule as a product ($-\text{H}_2\text{O}$) in each oligomerization step, thereby reducing O/C ratios in the higher order oligomers.

Figures 2a,b show that CCS values of PSOA oligomer ions observed in positive ionization mode are concentrated around the center line of the alcohols reference region. Meanwhile, CCS values of the LSOA positive oligomers are shifted below the center line. Figure S11 illustrates the quantitative assessment of the percent deviation of these two data sets measured in (+)ESI from the carboxylic acid and long-chain alcohols reference area. A majority of CCS for PSOA and LSOA are 2 - 8% below the carboxylic acid center reference line with some PSOA monomers having CCS values closer to the centerline. Approximately 48% of the CCS for PSOA positive oligomer ions fall 1-4% above the center line, while 55% of the CCS for the analogous LSOA species fall 1-4% below the line. The observed results indicate that positive oligomer ions of PSOA have systematically higher CCS values than their LSOA counterparts. This is consistent with the expected larger three-dimensional structures of PSOA oligomer products, which retain four-membered cyclobutane rings of the α-pinene monomeric precursors (see Scheme I) making the oligomeric products too rigid to fold into compact conformer structures. In contrast, all LSOA products have open-chain structures capable of folding into much more compact conformers, which result in comparably smaller CCS values. In negative ionization mode, the CCS values of monomers from LSOA and PSOA mixtures lie within the alcohols reference area, whereas CCS values of the oligomer ions lie 6 - 8% above the long-chain alcohols center line as shown in Figures 2c.d. As will be discussed in the next sections, these results are consistent with structural differences of negative and positive ions formed in the ESI source.

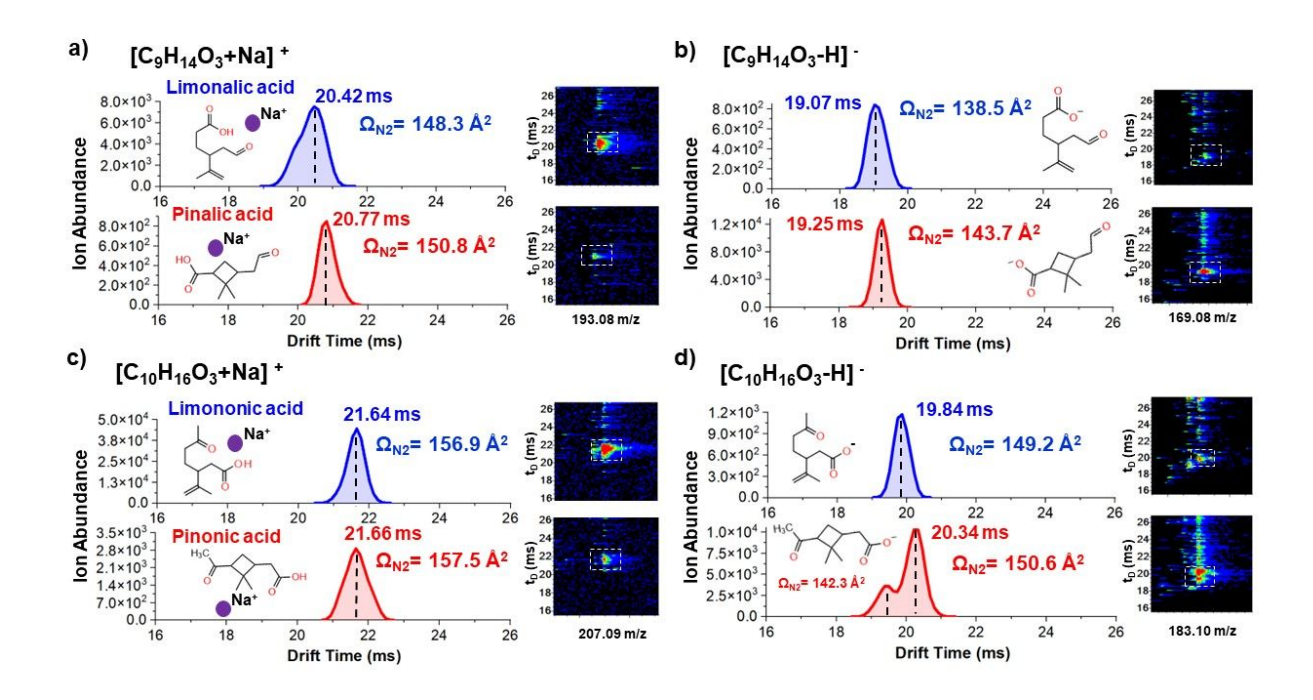


Figure 3. Drift time distributions for selected ions of a-b) $C_9H_{14}O_3$ and c-d) $C_{10}H_{16}O_3$ monomeric products of LSOA (blue) and PSOA (red) measured in the (+)ESI mode as [M+Na]⁺ adducts and in (-)ESI mode as [M-H]⁻ species, respectively. The experimental CCS (Ω_{N2}) are listed for each IM feature along with selected structure identities. The 2D heatmap insets are shown to the right of each drift spectrum for the measured IM-MS feature. Proposed structures and identities are shown along each panel.

Figures 3 and 4 illustrate drift time (DT) distributions of representative monomer and dimer ions observed in LSOA and PSOA mixtures along with their characteristic drift times (ms) and CCS values (Å²). Molecular structures are shown for a subset of the IM-MS detected features based on previous studies. 28,110 The 2D drift time versus m/z heatmaps characteristic for each of the selected IM features are shown in the right panels to illustrate their experimental detection. Figures 3a,b and 3c,d show the DT distributions for the monomer ozonolysis products: limonalic and pinalic acid isomers (C₉H₁₄O₃) and limononic and pinonic acids (C₁₀H₁₆O₃) detected as [M+Na]⁺ and [M-H]⁻ ions, respectively. The C₉H₁₄O₃ species of LSOA and PSOA observed in positive mode (Figure 3a), have similar DT distributions. However the peak shape for the LSOA feature exhibits a shoulder on the more compact side, while the peak of the PSOA constituent has a shoulder on the more extended side of the DT distributions. This observation indicates that although the major fraction of structures with this composition have similar CCS values, LSOA contains isomers with more compact structures and PSOA contains isomers with more extended structures. In contrast, negative mode DT distributions of both isomers (Figure 3b) are narrower and exhibit nearly identical DT distributions indicative of only one family of structures in both LSOA and PSOA ionized in negative mode. It is plausible that only one isomer with the

deprotonated carboxylic acid group contributes to the DT distribution observed negative mode. Meanwhile, a mixture of isomers containing ketone and aldehyde groups is likely ionized in positive mode. Ketolimonaldehyde is a representative species with this composition known to be present in LSOA.¹¹¹ This molecule possesses two ketones and one aldehyde group and forms compact adduct ion with Na⁺ in (+)ESI mode. It is likely that ketolimonaldehyde contributes to the shoulder peak with lower DT observed for the LSOA feature (Figure 3a). Meanwhile, at least one or two isomers such as limonalic and norlimononic acids with one carboxylic acid group²³ have more extended structures observed in the DT distribution (Figure 3a).

The positive mode DT distribution of $C_{10}H_{16}O_3$ (Figure 3c) in the PSOA sample has a larger peak width than the corresponding feature in the LSOA sample. The broad DT distribution indicates the presence of multiple of isomers of $C_{10}H_{16}O_3$ in the PSOA mixture. Previous study investigating isomers of $C_{10}H_{16}O_3$ generated in the ozonolysis of α -pinene, reported the presence of up to three individual peaks for $C_{10}H_{16}O_3$ species ionized as Na⁺ adducts. Herefore the two small shoulder peaks on both the compact and extended side of DT distribution may be related to isomers or conformers of pinonic acid + Na⁺, while abundant peak centered at 21.66 ms most likely corresponds to pinonic acid. On the other hand, we observe two distinct features (19.5 ms and 20.3 ms) in the DT distributions of $C_{10}H_{16}O_3$ in PSOA (Figure 3d) in negative mode. We attribute these peaks to two IM features to conformers of pinonic acid, which are supported by theoretical CCS calculations summarized in Table S1. The presence of two distinct peaks in the DT distribution indicate that two conformational isomers of pinonic acid are likely separated in IM-MS. The DT distributions for LSOA monomers appear to be similar in positive and negative modes (Figure 3c and 3d) suggesting only one type of the $C_{10}H_{16}O_3$ isomer in LSOA was ionized, corresponding to limononic acid.

The experimental CCS values for monomers of [M+Na]⁺ are systematically larger by 5 – 7% than CCS of their [M–H]⁻ counterparts. These results are supported by TMLJ predictions shown in Table S1. The larger cross-section of [M+Na]⁺ may be attributed to the size of the sodium cation coordinated to the analytes observed as positive ions,^{84,112} which increases the surface area of the ions. These observations are consistent with the results of previous study,⁸⁴ in which an increase in the CCS with mass of inorganic reagent ions (e.g. Na⁺, Li⁺, and K⁺) was observed for the ozonolysis products of α -pinene. These results are also consistent with [M+Na]⁺ adducts of carbonyl-containing phthalates measured in previous studies.^{113,114} The CCS values for Na adducts were 4.3% larger than the protonated counterparts in their work.¹¹⁴

While the DT distributions and identities for monomers (Figure 3) show interesting results, the DT distributions for the dimer ozonolysis products (Figure 4) are more complex. Figures 4a,b and 4c,d show the DTs for the dimer ozonolysis products: $C_{18}H_{28}O_7$ and $C_{19}H_{28}O_8$ detected as [M+Na]⁺ and [M-H]⁻ ions, respectively. The peak shape for the PSOA feature in Figure 4a shows a prominent peak at ~ 25.8 ms, followed by broadened shoulder peak on the more extended side of the DT, whereas the LSOA feature shows one small shoulder peak on the compact side of the DT peak (< 25.8 ms) and a broader shoulder peak on the extended side (> 25.8 ms). It is plausible

that at least two and three peaks contribute to the PSOA and LSOA DT distributions, respectively. However, the DT distributions measured in (–)ESI mode (Figure 4b) are not significantly different, where the LSOA feature is slightly more broadened than PSOA and both peaks are slightly narrower than the corresponding features observed in the positive mode. Similar observations can be made for C₁₉H₂₈O₈ dimer features in Figures 4c,d. From the peak shapes measured for (+/–) ESI modes, it appears that there are several structures of the organic compounds with different ionizable groups that were not ionized in one mode or the other. It is plausible that different structural isomers were selectively ionized in negative mode corresponding to molecules with more than one carboxylic acid group, whereas isomer ionized in positive mode likely contain carbonyl containing functional groups or conformers of [M+Na]⁺ ions. In addition, the relatively broad DT distributions for LSOA features shown in Figure 4 are consistent with a larger number of structural isomers known to be formed in ozonolysis of limonene as compared to α-pinene. Therefore systematic studies focused on targeted analysis of structural isomers in complex SOA need to account for differences in their ionization selectivity and physicochemical properties.^{11,115}

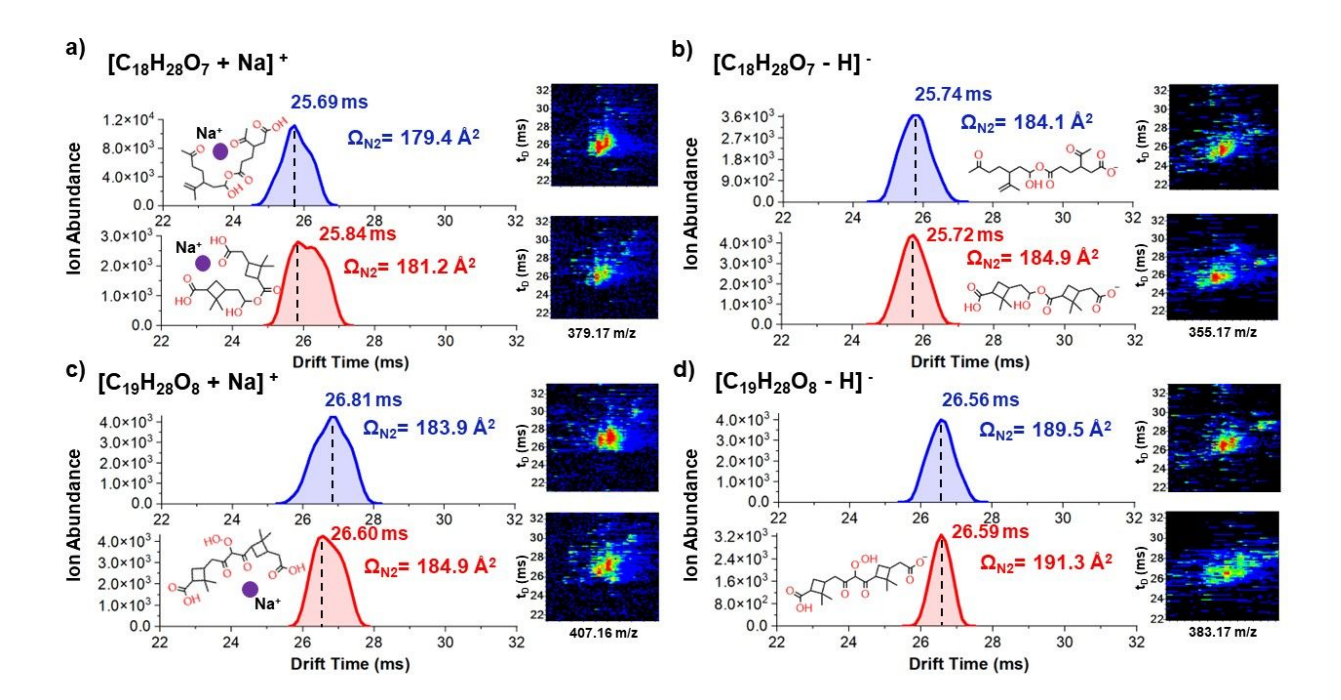


Figure 4. Drift time distributions obtained for selected ions of a–b) $C_{18}H_{28}O_7$ and c–d) $C_{19}H_{28}O_8$ dimeric products of LSOA (blue) and PSOA (red) measured in the (+)ESI mode as [M+Na]⁺ adduct and (–) ESI mode as [M–H]⁻ species, respectively. The experimental CCS (Ω_{N2}) are shown for each IM feature along with selected structure identities. The 2D heatmap insets are shown to the right of each drift spectrum for the measured IM-MS feature. Proposed dimeric structures are shown for few panels.

The CCS values of $[M+Na]^+$ and $[M-H]^-$ ions of C_{18} and C_{19} oligomer isomers in Figure 4 show different trends than what was observed for the C_9 and C_{10} monomers in Figure 3. The CCS values of the $[M+Na]^+$ ions are systematically smaller than those obtained for $[M-H]^-$ ions.

This observation is somewhat counterintuitive because it implies that $[M+Na]^+$ oligomer ions with larger m/z values exhibit smaller CCS than $[M-H]^-$ counterparts of lower m/z values. Figures 5a,b show CCS versus m/z plots derived for LSOA and PSOA species detected in (+/-)ESI modes along with linear regression lines for each of the four measurements. Here, we report deviation as percent of the CCS difference (Δ CCS%) between the linear regression lines and $[M-H]^-$ and $[M+Na]^+$ data sets, respectively. The plots indicate that CCS values of the deprotonated oligomers are 3 – 7% larger than their sodiated adducts, consistent for all oligomers within 300 – 600 m/z range. Figures 5c,d illustrate representative energy minimized DFT calculated structures of $[M+Na]^+$ and $[M-H]^-$ corresponding to $C_{19}H_{28}O_7$ and $C_{19}H_{28}O_8$ dimer products in LSOA and PSOA mixtures. The energy minimized structures for $[M+Na]^+$ ions indicate folding of the dimers when sodium is coordinated with three carbonyl oxygens, rather than one or two carbonyl oxygen atoms predicted for the monomer structures from DFT calculations.

The deprotonated molecules of both selected dimers exhibit slightly elongated structures which result in larger CCS values. DFT calculations indicate similar trends for few additional species summarized in Table S2. The number of carbonyl groups in the molecules is expected to increase for the high molecular weight oligomers (dimers + trimers) structures. It is reasonable to assume that the increase in Δ CCS% scales with an increase in the number of oxygen groups in the oligomer compositions. However, not all deprotonated oligomers exhibit similar elongated conformations. For example, pinonyl-pinyl ester $(C_{19}H_{28}O_7)$ product of PSOA has two carboxylic acid groups in the structure, 18 which facilitate the formation of the proposed compact circular conformation shown in Table S2 due to intramolecular hydrogen (H) bonding (O – H···O–)⁵⁷ at the terminal carboxyl end groups. The CCS of the deprotonated molecule is $185.4 \pm 0.3 \text{ Å}^2$, whereas the sodiated adduct exhibits a slightly larger CCS value of $187 + 2 \text{ Å}^2$ at the first peak of DT distribution as shown in Figure S12, however the DT of the broad shoulder peak for [M+Na]⁺ ion shifts to extended configuration with a CCS value of 189.8 \pm 2 Å². This suggests that the deprotonated conformer is slightly more compact than detected sodium adduct in the positive mode. These results are consistent with the corresponding experimental CCS values obtained in a previous report.⁷⁵

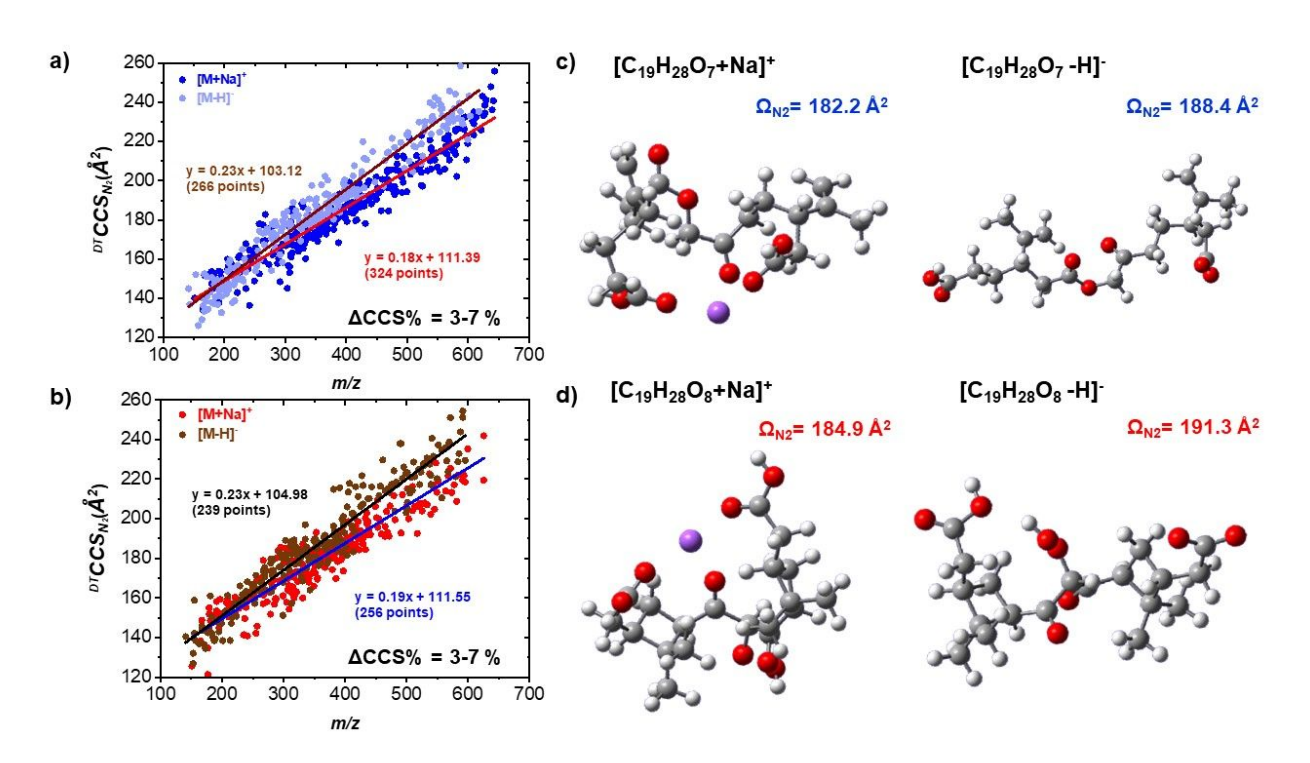


Figure 5. Plots of experimental CCS vs. m/z for a) LSOA and b) PSOA. The closed circle data points represent [M+Na]+ (blue: LSOA; red: PSOA) and [M-H]- (light blue: LSOA; maroon: PSOA)... The linear fits to each of the datasets are shown with the experimental slope equation in the form of 'y = mx + b' determined from the fits. The number of datapoints comprising experimental CCS are reported for statistics. Representative DFT geometry optimized ion structures are shown for c) $C_{19}H_{28}O_7$ and d) $C_{19}H_{28}O_8$ dimers detected as [M+Na]+ and [M-H]- ions, respectively. The experimental CCS are shown alongside 3D structures.

Notably, DFT calculations indicate the presence of multiple conformations of [M+Na]⁺ and [M–H]⁻ ions, in which Na⁺ is coordinated with different oxygenated groups and more than one carboxylic group can be deprotonated as illustrated in Table S2 for $C_{19}H_{28}O_7$ dimer. As the number of carbon atoms in the ions increases, the number of structural isomers and their conformers increases exponentially, leading to a high probability that multiple isomers contribute to the same IM feature. Plausible contributions of multiple isomers can be inferred from relatively broad IM features shown in Figures 3a,c and 4a,c. Therefore, we conclude that, in many cases, the resolving power of the drift tube IM separation (R_p) is insufficient for resolving the contributing isomers.¹¹⁶

To improve the IM resolution, we employed a recently developed methodology of temporal multiplexing and HRdm post-acquisition data reconstruction. ^{58,89} This method codes the IM-MS instrument to trap and release multiple discrete ion packets from the second stage grid of the trapping ion funnel over the 70 ms drift time range of experiment. Whereas the single pulse technique is limiting due to the time required to wait for the next sequential pulse in the IM cycle, which is one pulse every ~ 40 ms. Figure 6a illustrates the overall data post-processing workflow,

beginning with IM multiplexing experiments followed by standard demultiplexing of the acquired data into a reconstructed drift spectra. Obtained spectra are then deconvoluted by the HRdm software, revealing the contributions of individual isomer peaks. The overlaid drift spectrum in Figure 6a compares the demultiplexed drift time distribution of $[C_{19}H_{32}O_6+Na]^+$ ion (black trace) along with the individual spectral components (purple traces) obtained using HRdm deconvolution IM processed and the corresponding R_p values. The HRdm approach reveals additional IM features that could not be resolved using traditional single-pulse IM measurements.

Figures 6b,c show the demultiplexed IM spectra of the monomer [C₉H₁₄O₃+Na]⁺ and the dimer [C₁₈H₂₈O₇+Na]⁺ ions (IM features from Figure 3 & 4) from LSOA mixture and their HRdm-IM deconvoluted features with their corresponding R_p and CCS values, respectively. Plausible structures are shown for the resolved features based on literature report¹¹¹ and our modeling results. Specifically, out of six HRdm-IM deconvoluted features contributing to the drift time distribution of the [C₉H₁₄O₃+Na]⁺ ion, three peaks at 18.8, 19.1, and 19.4 ms are very abundant. These three features likely correspond to structural isomers of ketolimonaldehyde, limonalic acid, and norlimononic acid, which arise from the O₃-initiated oxidation of limonene at the two double bond locations in the structure. 111,117-119 The CCS values of the corresponding three isomers are different by at least 2 Å² from each other, or by $\Delta CCS\% \sim 2\%$ on the relative scale. The tentative identification of the LSOA oxidation product isomers is inferred based on the theoretical CCS values computed using IMoS (see Table S3), which match within $\sim 2-3\%$ to experimental CCS values. The other three HRdm-IM deconvoluted features are ether additional structural isomers or conformers, which could not be unambiguously assigned. Similarly, the [C₁₈H₂₈O₇+Na]⁺ dimer ion reveals at least six prominent HRdm features with CCS values differing by $2-7~\text{Å}^2$ from each other.

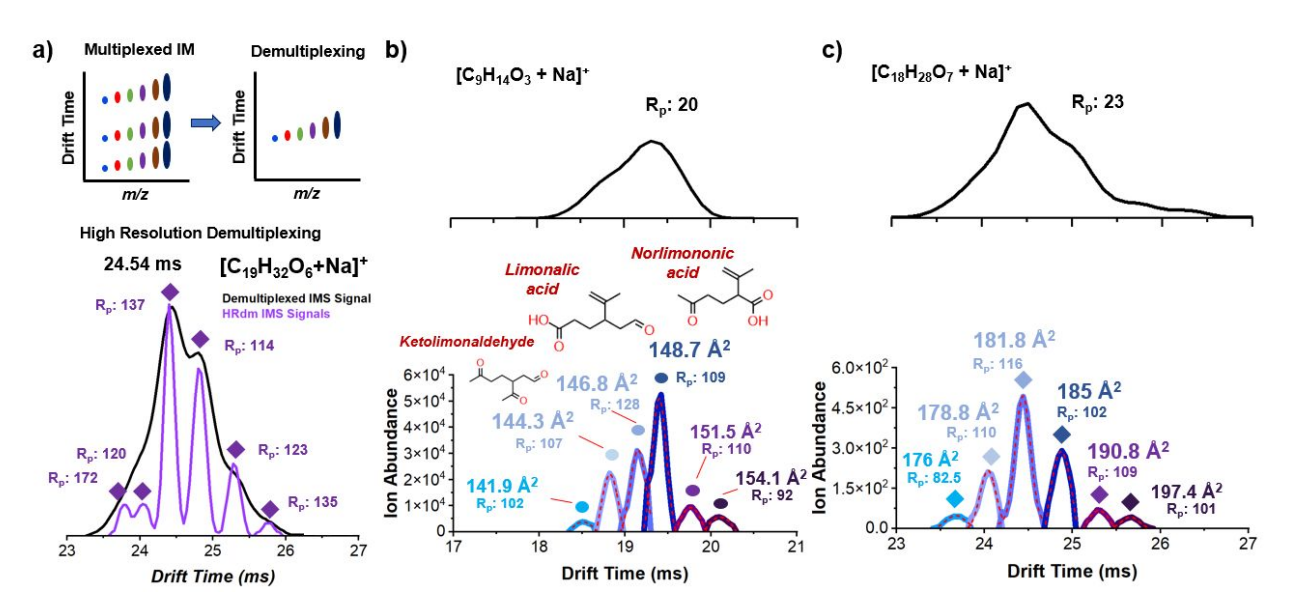


Figure 6. a) Illustrative description of IM multiplexing experiment, demultiplexing and high resolution demultiplexing (HRdm) workflow followed by illustrative example of HRdm processing of demultiplexed IM spectrum (overlaid) for the $[C_{19}H_{32}O_6+Na]^+$ ion in LSOA dataset. Drift spectra and extracted HRdm

features of the 4-bit ion-multiplexed data for b) $[C_9H_{14}O_3+Na]^+$ and c) $[C_{18}H_{28}O_7+Na]^+$ ions with their corresponding single-peak resolving power (Rp) and collision-cross section (CCS, Ų) values measured using the single-field method. Plausible structures are shown for each of the identified IM features based on literature reports 111,117–119 and theoretical CCS calculations. All HRdm IM spectra were processed at the highest processing level.

Figure 7 shows additional results of the HRdm-IM deconvolution for selected ions from LSOA and PSOA mixtures, which illustrates common level of complexity of the IM-MS data. For each of the common IM-MS features, HRdm method resolves 2-4 coincidental isomers comprising monomers (Figures 7a-c) and 4-6 isomers comprising dimers (Figures 7d-i). Although standard IM features have typical drift peak widths of 0.4-0.7 ms for monomers and 0.9-1.9 ms for dimers, their HRdm deconvoluted components show much narrower peaks with $\Delta t \sim 0.15$ ms. To validate the presence of isomeric species detected after the HRdm-IM deconvolution of the multiplexed IM-MS data, we performed an LC-HRMS experiment. Figures S13-S14 compare the deconvoluted drift time distributions of the $C_{20}H_{32}O_6$ dimer in LSOA and $C_{10}H_{16}O_4$ monomer in PSOA measured as $[M+Na]^+$ ions with extracted ion chromatograms of these ions observed using LC-HRMS. The comparison suggests that that the HRdm-deconvoluted peaks correspond to structural isomers rather than to conformers. These results demonstrate that HRdm-IM-MS may be used for the detection of isomeric SOA components in a significantly shorter data acquisition time (0-40 ms) in comparison with LC-MS (20 min-1 hr) per sample.

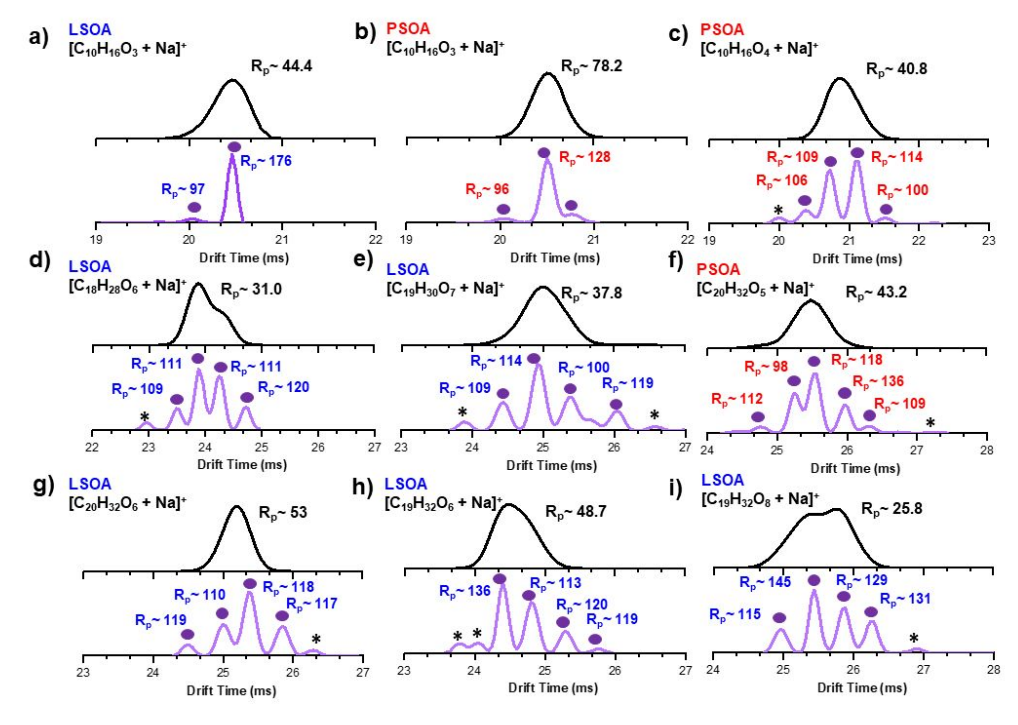
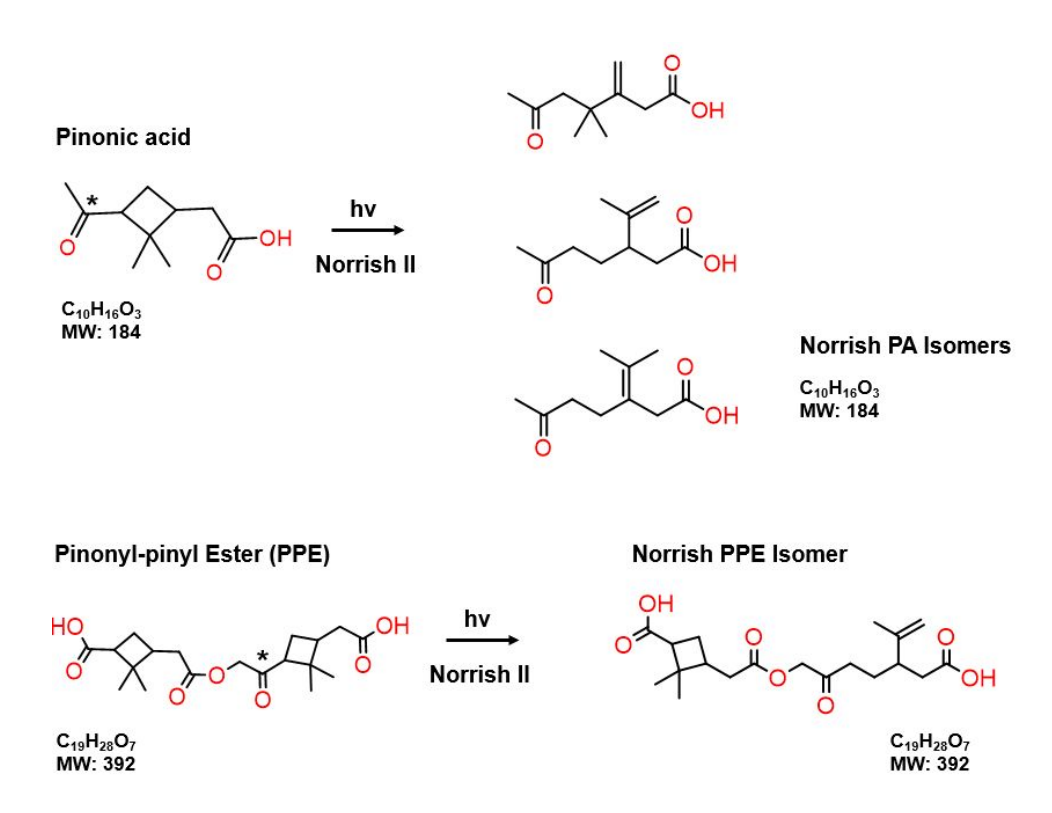


Figure 7. IM spectra of the several isomer systems in LSOA (blue legends) and PSOA (red legends) investigated in this work related to the monomers a) limononic acid ($C_{10}H_{16}O_3$), b) pinonic acid ($C_{10}H_{16}O_3$), c) OH-pinonic acid ($C_{10}H_{16}O_4$) and dimers d–i) $C_{18}H_{28}O_6$, $C_{19}H_{30}O_7$, $C_{20}H_{32}O_5$, $C_{20}H_{32}O_6$, $C_{19}H_{32}O_6$, and $C_{19}H_{32}O_8$, respectively. The top panel in the drift spectra represent the standard demultiplexed IM spectra (black trace), while bottom panels show the HRdm peak deconvoluted IM spectra (purple trace) with their corresponding R_p values in respective coloring legends. All HRdm IM spectra were processed at the highest processing setting. The HRdm deconvoluted components show much narrower peaks with $\Delta t \sim 0.15$ ms versus 0.4-0.7 ms in standard demultiplexing. The peaks that are marked with an asterisk (*) are postprocessing data artifacts lower than 5% of the total ion signal.

To demonstrate the utility of IM-MS for studying chemical transformations of isomeric SOA components, we conduct case experiments comparing PSOA components in the original and photolyzed mixtures. Photochemical aging of SOA in the presence of solar irradiation is an important pathway for oxidation and degradation of organic constituents resulting in transformations in their chemical and physical properties. 90,120,121 In particular, PSOA monomeric components such as pinonic acid (PA), pinic acid, pinonaldehyde and their multi-functional oligomers possess carbonyl groups susceptible to photolysis via Norrish I & II pathways. 110,122,123 Scheme II illustrates the Norrish Type II reaction of pinonic acid (PA) and pinonyl-pinyl ester (PPE) components of PSOA, which results in photoisomerization. In this reaction, the 1,5-shift of a hydrogen atom to the photoexcited carbonyl group results in ring opening of the molecule. 110



Scheme II. Norrish Type II photochemical isomerization of pinonic acid (PA) and pinonyl-pinyl ester (PPE) dimer product in PSOA mixture. The (*) denotes the photoexcited carbonyl group in the structures. Product isomers for PA and PPE are shown based on literature reports¹¹⁰ and proposed structure following Norrish II splitting/ring-opening mechanism.¹²²

In our experiments, PSOA aqueous mixtures were irradiated in a custom-built 310 nm photoreactor (see Supplementary Note 2), where the solution was irradiated for 60 min at a constant photon flux (F_{LED}). Figure 8a,b show the IM drift spectra for [M–H]⁻ ions corresponding to PA ($C_{10}H_{16}O_3$) and PPE ($C_{19}H_{28}O_7$) species. The IM spectra of the corresponding [M–H]⁻ ions identified in LSOA mixture, limononic acid ($C_{10}H_{16}O_3$) and the dimer ester product ($C_{19}H_{28}O_7$), are shown for comparison. The characteristic value of CCS for PA detected as [$C_{10}H_{16}O_3$ –H]⁻ ion in the unphotolyzed PSOA is 150.6 Å². In the photolyzed PSOA sample, the CCS value of the [$C_{10}H_{16}O_3$ –H]⁻ species decreases to 148.7 Å², a value comparable to the CCS of the limononic acid (LA) isomer (149.2 Å²). This change in the CCS value is consistent with the PA to LA photoisomerization shown in Scheme II. The Norrish PA isomeric product is more compact and more mobile as a result of the cleavage of the rigid cyclobutane ring. The shape of the IM feature corresponding to the isomer product exhibits significant peak broadening, which suggests formation of multiple isomers, in line with literature reports.¹¹⁰

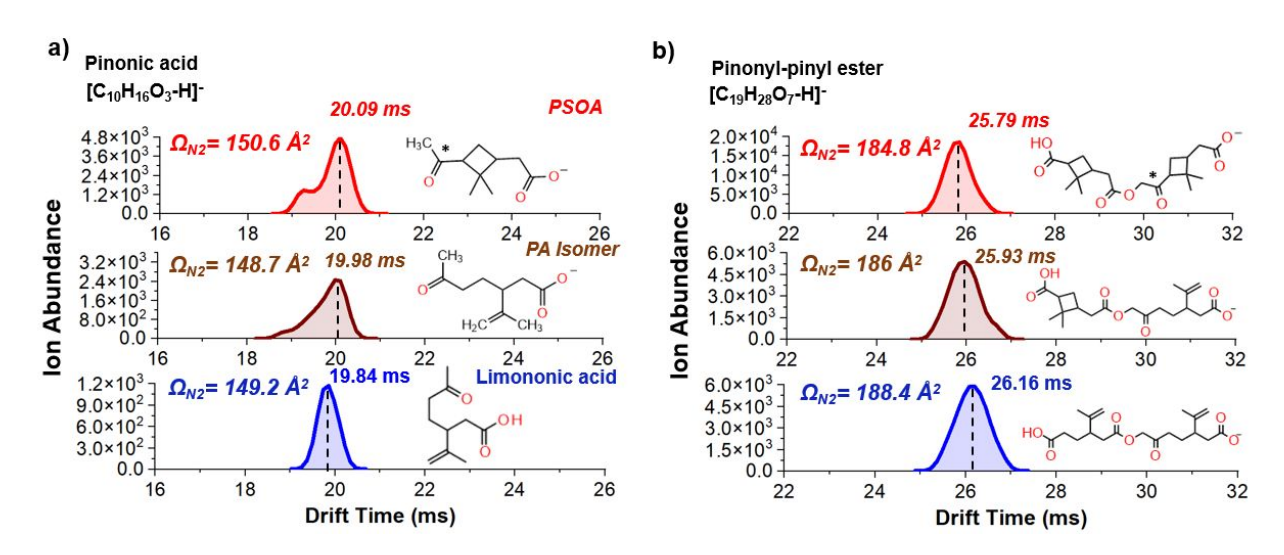


Figure 8. IM drift spectra representing the IM features for a) $C_{10}H_{16}O_3$ and b) $C_{19}H_{28}O_7$ measured as [M-H]⁻ ion for PSOA (red), LSOA (blue), and the photochemical Norrish II product isomer (maroon) arising from the aqueous photolysis of bulk solution containing PSOA mixture. The experimental CCS (Ω_{N2}) is shown for each IM feature along with proposed structures.

Similarly, the PPE dimer detected as the [C₁₉H₂₈O₇–H]⁻ ion in the unphotolyzed PSOA has a CCS value of 184.8 Å². In the photolyzed sample, the CCS value of the isomer product increases to 186 Å², also consistent with opening of the cyclobutane ring, resulting in a less compact structure. However, the isomer product is still significantly different from the open-chain reference dimer (CCS = 188.4 Å²) observed in the LSOA mixture, which suggests that the photolyzed product likely retains one cyclobutane ring. The analytical detection and characterization of these reactants and Norrish II products were confirmed using LCMS measured in the (-)ESI mode as shown in the extracted ion chromatograms (EIC) in Figure S15. Additional IM-MS characterization of the photolytic isomerization of selected PSOA components is shown in Figures S16 and S17. The CCS measurements are consistent with the expected Norrish II photochemical pathway as the photolyzable ketone group on one side of the dimer ester molecule (denoted as *) in PSOA can participate in the ring-opening and rearrangement to yield the expected isomers shown in Figure 8b. Our results demonstrate that IM-MS may be used to measure structural changes associated with photochemical reactions of individual aerosol components.

Conclusions

The chemical composition and variability of isomer structures in PSOA and LSOA mixtures were examined using IM-MS metrology platform. We developed a ^{DT}CCS_{N2} (Å²) library of structural isomers in complex LSOA and PSOA mixtures. The ^{DT}CCS_{N2} values indicate that both LSOA and PSOA constituents contain carboxylic acid functional groups and polymeric-like

structures for the dimeric and trimeric species. Several of the monomeric and dimeric SOA species in PSOA exhibited slightly larger (1-4%) CCS values than their LSOA counterparts. This observation reflects the larger gas-phase ion structures of PSOA components due to the presence of rigid cyclobutane rings. The average $^{DT}CCS_{N2}$ values for monomeric SOA components measured as $[M+Na]^+$ ions are 3-6% higher than those of their $[M-H]^-$ counterparts. Meanwhile, dimeric and trimeric isomer components in both samples showed an inverse trend with the $^{DT}CCS_{N2}$ values of $[M-H]^-$ ions being 3-7% higher than those of their $[M+Na]^+$ counterparts. Therefore, the 3D configuration of the ions formed during ESI are dependent on the mode of ionization polarity.

The incorporation of the 2D $^{\rm DT}CCS_{\rm N2}({\rm Å}^2)-m/z$ space with representative molecular-class trend lines compiled from literature 82,83 enables practical assessment of structural isomers in complex SOA mixtures and may be used to infer on potential aging reactions in aerosols. 45,82 For example, reactions of biogenic VOCs with NOx, 124 NO3 radicals, 125 or ammonia 11 may result in the formation of functionalized nitrate or amino groups in the structures. This may lead to an increase in the experimental CCS and fall into separate structural class in the 2D $^{\rm DT}CCS_{\rm N2}({\rm Å}^2)-m/z$ projected space. 83 Formation of organosulfate compounds in PSOA from the evaporative drying in presence of sulfuric acid, 126 is expected to also increase the CCS. Additionally, the discrimination between the ring-retained, ring-opening, and isomeric products of toluene derived SOA under OH oxidation and high/low NO_X is also important to distinguish in complex SOA mixtures. 127,128 Structural characterization of water-soluble metal-organic complexes 129,130 involving small carboxylic acids with iron (Fe³⁺) from SOA, environmental samples, and cloud water can also be performed using IM-MS for untargeted analyses. More IM studies are needed to expand accurate CCS measurements to a broad range of atmospheric molecules relevant to SOA formation and aging.

The broadening in drift time of separated peaks measured in IM–MS experiments relates to a combination of isomers that were poorly resolved from single pulse IM measurements. The application of an IM multiplexing/HRdm approach^{58,89} helped to distinguish between individual isomer ions detected in the SOA mixtures. We demonstrate successful application of the HRdm post-processing for multi-component isomeric mixtures in SOA to help reveal complex IM peaks that resemble different structural ensembles of the analyte ions. Future studies investigating complex structural isomers in SOA using high resolution IM separations^{131,132} would be valuable for this application. Last, we demonstrated the potential use of IM-MS for studying photochemical aging of single molecule components in complex SOA mixtures. The IM methods can be applied to study single-molecule structural changes associated with aerosol aging.

While this work presents advantages and strengths of the IM-MS experiments employed for SOA characterization, several areas for further developments need to be noted. First, without the incorporation of an LC separation or a sample purification step (e.g. solid-phase extraction)^{39,89,133} to IM-MS workflow, ion suppression may effect sensitive detection of individual components in complex SOA mixtures. Incorporating LC separation stage to IM-MS

workflows will also improve quantitative capability for SOA characterization. Second, programming tandem IM multiplexing/HRdm data analysis workflows are excellent for very low concentrated organic components in the solution. However, it cannot be applied for LC-IM-MS workflows and does not perform well for higher concentrated components in the samples. 58,88

Accurate measurements of CCS in IM-MS experiments benefit from the complementary use of stepped-field and single-field data acquisition methods. While both methods can be employed in the direct infusion IM-MS experiments presented here, experiments with the LC separation stage added can only use the single-field method. Therefore, design of future IM-MS studies should consider various tradeoffs of the methods and data interpretations discussed in this work. Last, comparative analysis of either commercial or synthesized²⁸standards may greatly facilitate assessment of the structure-specific SOA products, based on the interpretation of their IM-MS spectra.

The molecular and structural-level information afforded by CCS measurements for SOA components may be useful for predicting the physical properties of individual compounds such as the molecule-specific glass transition temperature (T_g) and viscosities (η) .¹³⁴ General understanding of the structural effects of SOA components on T_g is important to aid in the evaluation of the aerosol phase state and their contributions to the bulk viscosity of SOA particles. The structures of common SOA components contain carboxylic (-COOH), ester (-C(=O)OR), alcohol (-OH), ketone (-C(=O)R, ether (-COR), and aldehyde (-C(=O)H) functional groups, which influence their viscosities and volatility. The volatility of the components will in turn influence the gas-particle partitioning in SOA. The incorporation of structural information provided by IM-MS experiments may improve the accuracy of estimating T_g and η of SOA. The incorporation of structural information provided by IM-MS experiments may improve the accuracy of estimating T_g and η of SOA. The incorporation of structural information provided by IM-MS experiments may improve the accuracy of estimating T_g and η of SOA. The incorporation of structural information provided by IM-MS experiments may improve the accuracy of estimating T_g and η of SOA. The incorporation of structural information provided by IM-MS experiments may improve the accuracy of estimating T_g and η of SOA. The viscosity is also predicted to increase for individual species in SOA.

Supporting Information

Supplementary Notes 1–7 provide descriptions for BVOC oxidation and SOA generation experiments, aqueous photolysis and chemical actinometry calculations, IM-Q-TOFMS metrology, DI-HRMS, and LC-HRMS methodology and data analysis, IM-MS data processing and analysis, and computational chemistry and ion mobility theoretical calculations. Additional figures (S1–S17) illustrating supplementary notes, IM-MS and HRMS results of SOA characterization are shown. Summary tables (S1–S3) report theoretical DFT and TMLJ calculations for select components.

A full list of all CCS values, m/z, and formula assignments in IM-MS experiments are summarized in a 'IM MS CCS Data SOA.xlsx' file.

Author Contributions. C.P.W, J.L, and A.L designed the overall project framework, experiments, and manuscript logic. C.P.W and A.C.M conducted aerosol generation experiments, particle collections, and measurements. C.P.W performed sample extractions and extract preparations. C.P.W. and D.M.S performed the IM-Q-TOF experiments and method development. C.P.W. performed the HRMS and LC-HRMS molecular characterization experiments and led data analysis with assistance from D.M.S, Y.H., J.R, and A.D. Theoretical quantum molecular calculations were performed by C.P.W guided by L.V.S. C.P.W, J.L, and A.L. wrote the manuscript with contributions from all co-authors.

Competing Interests. The authors declare that they have no conflict of interest.

Acknowledgments. We acknowledge support from the startup funds allocated to A. Laskin by the Department of Chemistry at Purdue University and partial support from the National Science Foundation award AGS-2039985 at the time of this manuscript preparation. D.M.S. acknowledges support from the National Science Foundation Graduate Research Fellowship under Grant No. (DGE-1333468). A.C.M acknowledges support from the National Science Foundation Graduate Research Fellowship under Grant No. DGE-1333468. We would like to acknowledge Dr. John Fjelsted from Agilent Technologies for providing access to HRdm 2.0 software and expertise relevant in the data interpretation for this work. We also acknowledge Dr. Carlos Larriba-Andaluz for advice on theoretical CCS computations in IMoS software. This research was supported in part through computational resources provided by Information Technology at Purdue University.

Author Information

Corresponding Author

* Alexander Laskin – Department of Chemistry, Purdue University, Indiana 47906, United States; orcid.org/0000-0002-7836-8417; Email: alaskin@purdue.edu

Contributing Authors

Christopher P. West – Department of Chemistry, Purdue University, Indiana 47906, United States; orcid.org/0000-0001-9337-2820

Daniela Mesa Sanchez – Department of Chemistry, Purdue University, Indiana 47906, United States; https://orcid.org/0000-0002-4499-7872

- **Ana C. Morales** Department of Chemistry, Purdue University, Indiana 47906, United States; orcid.org/0000-0001-6969-2883
 - **Yun-Jung Hsu** Department of Chemistry, Purdue University, Indiana 47906, United States
- **Jackson Ryan** Department of Chemistry, Purdue University, Indiana 47906, United States
 - **Andrew Darmody** Department of Chemistry, Purdue University, Indiana 47906, United States; https://orcid.org/0000-0002-7749-397X
- **Lyudmila V. Slipchenko** Department of Chemistry, Purdue University, Indiana 47906, United States
 - **Julia Laskin** Department of Chemistry, Purdue University, Indiana 47906, United States; https://orcid.org/0000-0002-4533-9644

References:

- (1) Hallquist, M.; Wenger, J. C.; Baltensperger, U.; Rudich, Y.; Simpson, D.; Claeys, M.; Dommen, J.; Donahue, N. M.; George, C.; Goldstein, A. H.; Hamilton, J. F.; Herrmann, H.; Hoffmann, T.; Iinuma, Y.; Jang, M.; Jenkin, M. E.; Jimenez, J. L.; Kiendler-Scharr, A.; Maenhaut, W.; McFiggans, G.; Mentel, T. F.; Monod, A.; Prévôt, A. S. H.; Seinfeld, J. H.; Surratt, J. D.; Szmigielski, R.; Wildt, J. The Formation, Properties and Impact of Secondary Organic Aerosol: Current and Emerging Issues. *Atmospheric Chem. Phys.* **2009**, *9* (14), 5155–5236. https://doi.org/10.5194/acp-9-5155-2009.
- (2) Murphy, D. M.; Cziczo, D. J.; Froyd, K. D.; Hudson, P. K.; Matthew, B. M.; Middlebrook, A. M.; Peltier, R. E.; Sullivan, A.; Thomson, D. S.; Weber, R. J. Single-Particle Mass Spectrometry of Tropospheric Aerosol Particles. *J. Geophys. Res. Atmospheres* **2006**, *111* (D23). https://doi.org/10.1029/2006JD007340.
- Zhang, Q.; Jimenez, J. L.; Canagaratna, M. R.; Allan, J. D.; Coe, H.; Ulbrich, I.; Alfarra, M. R.; Takami, A.; Middlebrook, A. M.; Sun, Y. L.; Dzepina, K.; Dunlea, E.; Docherty, K.; DeCarlo, P. F.; Salcedo, D.; Onasch, T.; Jayne, J. T.; Miyoshi, T.; Shimono, A.; Hatakeyama, S.; Takegawa, N.; Kondo, Y.; Schneider, J.; Drewnick, F.; Borrmann, S.; Weimer, S.; Demerjian, K.; Williams, P.; Bower, K.; Bahreini, R.; Cottrell, L.; Griffin, R. J.; Rautiainen, J.; Sun, J. Y.; Zhang, Y. M.; Worsnop, D. R. Ubiquity and Dominance of Oxygenated Species in Organic Aerosols in Anthropogenically-Influenced Northern Hemisphere Midlatitudes. *Geophys. Res. Lett.* 2007, 34 (13). https://doi.org/10.1029/2007GL029979.
- (4) Pandis, S. N.; Harley, R. A.; Cass, G. R.; Seinfeld, J. H. Secondary Organic Aerosol Formation and Transport. *Atmospheric Environ. Part Gen. Top.* **1992**, *26* (13), 2269–2282. https://doi.org/10.1016/0960-1686(92)90358-R.
 - (5) Goldstein, A. H.; Galbally, I. E. Known and Unexplored Organic Constituents in the Earth's Atmosphere. *Environ. Sci. Technol.* **2007**, *41* (5), 1514–1521. https://doi.org/10.1021/es072476p.
 - (6) Guenther, A.; Hewitt, C. N.; Erickson, D.; Fall, R.; Geron, C.; Graedel, T.; Harley, P.; Klinger, L.; Lerdau, M.; Mckay, W. A.; Pierce, T.; Scholes, B.; Steinbrecher, R.; Tallamraju, R.; Taylor, J.; Zimmerman, P. A Global Model of Natural Volatile Organic Compound Emissions. *J. Geophys. Res. Atmospheres* **1995**, *100* (D5), 8873–8892. https://doi.org/10.1029/94JD02950.
 - (7) Guenther, A. B.; Jiang, X.; Heald, C. L.; Sakulyanontvittaya, T.; Duhl, T.; Emmons, L. K.; Wang, X. The Model of Emissions of Gases and Aerosols from Nature Version 2.1 (MEGAN2.1): An Extended and Updated Framework for Modeling Biogenic Emissions. *Geosci. Model Dev.* **2012**, *5* (6), 1471–1492. https://doi.org/10.5194/gmd-5-1471-2012.
 - (8) Atkinson, R.; Arey, J. Atmospheric Degradation of Volatile Organic Compounds. *Chem. Rev.* **2003**, *103* (12), 4605–4638. https://doi.org/10.1021/cr0206420.
- (9) Hatakeyama, S.; Izumi, K.; Fukuyama, T.; Akimoto, H.; Washida, N. Reactions of OH with α-Pinene and β-Pinene in Air: Estimate of Global CO Production from the Atmospheric Oxidation of Terpenes. *J. Geophys. Res. Atmospheres* **1991**, *96* (D1), 947–958. https://doi.org/10.1029/90JD02341.
 - (10) Isaksen, I. S. A.; Granier, C.; Myhre, G.; Berntsen, T. K.; Dalsøren, S. B.; Gauss, M.; Klimont, Z.; Benestad, R.; Bousquet, P.; Collins, W.; Cox, T.; Eyring, V.; Fowler, D.; Fuzzi, S.; Jöckel, P.; Laj, P.; Lohmann, U.; Maione, M.; Monks, P.; Prevot, A. S. H.; Raes, F.; Richter, A.; Rognerud, B.; Schulz, M.; Shindell, D.; Stevenson, D. S.; Storelvmo, T.; Wang, W.-C.; van Weele, M.; Wild, M.; Wuebbles, D. Atmospheric Composition Change: Climate—Chemistry Interactions. *Atmos. Environ.* 2009, 43 (33), 5138–5192. https://doi.org/10.1016/j.atmosenv.2009.08.003.
 - (11) Laskin, J.; Laskin, A.; Nizkorodov, S. A.; Roach, P.; Eckert, P.; Gilles, M. K.; Wang, B.; Lee, H. J. (Julie); Hu, Q. Molecular Selectivity of Brown Carbon Chromophores. *Environ. Sci. Technol.* **2014**, 48 (20), 12047–12055. https://doi.org/10.1021/es503432r.
 - (12) Nozière, B.; Kalberer, M.; Claeys, M.; Allan, J.; D'Anna, B.; Decesari, S.; Finessi, E.; Glasius, M.; Grgić, I.; Hamilton, J. F.; Hoffmann, T.; Iinuma, Y.; Jaoui, M.; Kahnt, A.; Kampf, C. J.; Kourtchev, I.; Maenhaut, W.; Marsden, N.; Saarikoski, S.; Schnelle-Kreis, J.; Surratt, J. D.; Szidat, S.;

- Szmigielski, R.; Wisthaler, A. The Molecular Identification of Organic Compounds in the Atmosphere: State of the Art and Challenges. *Chem. Rev.* **2015**, *115* (10), 3919–3983. https://doi.org/10.1021/cr5003485.
 - (13) J. Ziemann, P.; Atkinson, R. Kinetics, Products, and Mechanisms of Secondary Organic Aerosol Formation. *Chem. Soc. Rev.* **2012**, *41* (19), 6582–6605. https://doi.org/10.1039/C2CS35122F.
- Ehn, M.; Thornton, J. A.; Kleist, E.; Sipilä, M.; Junninen, H.; Pullinen, I.; Springer, M.; Rubach, F.; (14)Tillmann, R.; Lee, B.; Lopez-Hilfiker, F.; Andres, S.; Acir, I.-H.; Rissanen, M.; Jokinen, T.; Schobesberger, S.; Kangasluoma, J.; Kontkanen, J.; Nieminen, T.; Kurtén, T.; Nielsen, L. B.; Jørgensen, S.; Kjaergaard, H. G.; Canagaratna, M.; Maso, M. D.; Berndt, T.; Petäjä, T.; Wahner, A.; Kerminen, V.-M.; Kulmala, M.; Worsnop, D. R.; Wildt, J.; Mentel, T. F. A Large Source of Low-Nature Secondary Organic Aerosol. 2014. (7489),476-479. https://doi.org/10.1038/nature13032.
 - (15) Shrivastava, M.; Cappa, C. D.; Fan, J.; Goldstein, A. H.; Guenther, A. B.; Jimenez, J. L.; Kuang, C.; Laskin, A.; Martin, S. T.; Ng, N. L.; Petaja, T.; Pierce, J. R.; Rasch, P. J.; Roldin, P.; Seinfeld, J. H.; Shilling, J.; Smith, J. N.; Thornton, J. A.; Volkamer, R.; Wang, J.; Worsnop, D. R.; Zaveri, R. A.; Zelenyuk, A.; Zhang, Q. Recent Advances in Understanding Secondary Organic Aerosol: Implications for Global Climate Forcing. *Rev. Geophys.* **2017**, *55* (2), 509–559. https://doi.org/10.1002/2016RG000540.
- McFiggans, G.; Mentel, T. F.; Wildt, J.; Pullinen, I.; Kang, S.; Kleist, E.; Schmitt, S.; Springer, M.; Tillmann, R.; Wu, C.; Zhao, D.; Hallquist, M.; Faxon, C.; Le Breton, M.; Hallquist, Å. M.; Simpson, D.; Bergström, R.; Jenkin, M. E.; Ehn, M.; Thornton, J. A.; Alfarra, M. R.; Bannan, T. J.; Percival, C. J.; Priestley, M.; Topping, D.; Kiendler-Scharr, A. Secondary Organic Aerosol Reduced by Mixture of Atmospheric Vapours. *Nature* 2019, 565 (7741), 587–593. https://doi.org/10.1038/s41586-018-0871-y.
- Hammes, J.; Lutz, A.; Mentel, T.; Faxon, C.; Hallquist, M. Carboxylic Acids from Limonene Oxidation by Ozone and Hydroxyl Radicals: Insights into Mechanisms Derived Using a FIGAERO-CIMS. *Atmospheric Chem. Phys.* **2019**, *19* (20), 13037–13052. https://doi.org/10.5194/acp-19-13037-2019.
 - (18) Zhang, X.; McVay, R. C.; Huang, D. D.; Dalleska, N. F.; Aumont, B.; Flagan, R. C.; Seinfeld, J. H. Formation and Evolution of Molecular Products in α-Pinene Secondary Organic Aerosol. *Proc. Natl. Acad. Sci.* 2015, 112 (46), 14168–14173. https://doi.org/10.1073/pnas.1517742112.
 - (19) Lee, H. J. (Julie); Aiona, P. K.; Laskin, A.; Laskin, J.; Nizkorodov, S. A. Effect of Solar Radiation on the Optical Properties and Molecular Composition of Laboratory Proxies of Atmospheric Brown Carbon. *Environ. Sci. Technol.* **2014**, *48* (17), 10217–10226. https://doi.org/10.1021/es502515r.
- Wang, B.; O'Brien, R. E.; Kelly, S. T.; Shilling, J. E.; Moffet, R. C.; Gilles, M. K.; Laskin, A. Reactivity of Liquid and Semisolid Secondary Organic Carbon with Chloride and Nitrate in Atmospheric Aerosols. *J. Phys. Chem. A* **2015**, *119* (19), 4498–4508. https://doi.org/10.1021/jp510336q.
 - (21) Romonosky, D. E.; Laskin, A.; Laskin, J.; Nizkorodov, S. A. High-Resolution Mass Spectrometry and Molecular Characterization of Aqueous Photochemistry Products of Common Types of Secondary Organic Aerosols. *J. Phys. Chem. A* **2015**, *119* (11), 2594–2606. https://doi.org/10.1021/jp509476r.
 - (22) Hinks, M. L.; Brady, M. V.; Lignell, H.; Song, M.; Grayson, J. W.; Bertram, A. K.; Lin, P.; Laskin, A.; Laskin, J.; Nizkorodov, S. A. Effect of Viscosity on Photodegradation Rates in Complex Secondary Organic Aerosol Materials. *Phys. Chem. Chem. Phys.* **2016**, *18* (13), 8785–8793. https://doi.org/10.1039/C5CP05226B.
 - (23) Glasius, M.; Lahaniati, M.; Calogirou, A.; Di Bella, D.; Jensen, N. R.; Hjorth, J.; Kotzias, D.; Larsen, B. R. Carboxylic Acids in Secondary Aerosols from Oxidation of Cyclic Monoterpenes by Ozone. *Environ. Sci. Technol.* **2000**, *34* (6), 1001–1010. https://doi.org/10.1021/es990445r.
 - (24) Kourtchev, I.; Ruuskanen, T. M.; Keronen, P.; Sogacheva, L.; Maso, M. D.; Reissell, A.; Chi, X.; Vermeylen, R.; Kulmala, M.; Maenhaut, W.; Claeys, M. Determination of Isoprene and α-/β-Pinene

- Oxidation Products in Boreal Forest Aerosols from Hyytiälä, Finland: Diel Variations and Possible Link with Particle Formation Events. *Plant Biol.* **2007**, *9* (S 1), e1–e11. https://doi.org/10.1055/s-2007-964945.
- (25) Kourtchev, I.; Doussin, J.-F.; Giorio, C.; Mahon, B.; Wilson, E. M.; Maurin, N.; Pangui, E.; Venables, D. S.; Wenger, J. C.; Kalberer, M. Molecular Composition of Fresh and Aged Secondary Organic Aerosol from a Mixture of Biogenic Volatile Compounds: A High-Resolution Mass Spectrometry Study. *Atmospheric Chem. Phys.* **2015**, *15* (10), 5683–5695. https://doi.org/10.5194/acp-15-5683-2015.
 - (26) Zhang, X.; Lambe, A. T.; Upshur, M. A.; Brooks, W. A.; Gray Bé, A.; Thomson, R. J.; Geiger, F. M.; Surratt, J. D.; Zhang, Z.; Gold, A.; Graf, S.; Cubison, M. J.; Groessl, M.; Jayne, J. T.; Worsnop, D. R.; Canagaratna, M. R. Highly Oxygenated Multifunctional Compounds in α-Pinene Secondary Organic Aerosol. *Environ. Sci. Technol.* 2017, 51 (11), 5932–5940. https://doi.org/10.1021/acs.est.6b06588.
- L. Walser, M.; Desyaterik, Y.; Laskin, J.; Laskin, A.; A. Nizkorodov, S. High-Resolution Mass Spectrometric Analysis of Secondary Organic Aerosol Produced by Ozonation of Limonene. *Phys. Chem. Chem. Phys.* **2008**, *10* (7), 1009–1022. https://doi.org/10.1039/B712620D.
 - (28) Kenseth, C. M.; Hafeman, N. J.; Huang, Y.; Dalleska, N. F.; Stoltz, B. M.; Seinfeld, J. H. Synthesis of Carboxylic Acid and Dimer Ester Surrogates to Constrain the Abundance and Distribution of Molecular Products in α-Pinene and β-Pinene Secondary Organic Aerosol. *Environ. Sci. Technol.* **2020**, *54* (20), 12829–12839. https://doi.org/10.1021/acs.est.0c01566.
 - (29) Kenseth, C. M.; Huang, Y.; Zhao, R.; Dalleska, N. F.; Hethcox, J. C.; Stoltz, B. M.; Seinfeld, J. H. Synergistic O3 + OH Oxidation Pathway to Extremely Low-Volatility Dimers Revealed in β-Pinene Secondary Organic Aerosol. *Proc. Natl. Acad. Sci.* **2018**, *115* (33), 8301–8306. https://doi.org/10.1073/pnas.1804671115.
- 970 (30) Yasmeen, F.; Vermeylen, R.; Szmigielski, R.; Iinuma, Y.; Böge, O.; Herrmann, H.; Maenhaut, W.; Claeys, M. Terpenylic Acid and Related Compounds: Precursors for Dimers in Secondary Organic Aerosol from the Ozonolysis of α- and β-Pinene. *Atmospheric Chem. Phys.* **2010**, *10* (19), 9383–9392. https://doi.org/10.5194/acp-10-9383-2010.
- (31) Yasmeen, F.; Vermeylen, R.; Maurin, N.; Perraudin, E.; Doussin, J.-F.; Claeys, M.; Yasmeen, F.; Vermeylen, R.; Maurin, N.; Perraudin, E.; Doussin, J.-F.; Claeys, M. Characterisation of Tracers for Aging of α-Pinene Secondary Organic Aerosol Using Liquid Chromatography/Negative Ion Electrospray Ionisation Mass Spectrometry. *Environ. Chem.* 2012, 9 (3), 236–246. https://doi.org/10.1071/EN11148.
- (32) Kahnt, A.; Vermeylen, R.; Iinuma, Y.; Safi Shalamzari, M.; Maenhaut, W.; Claeys, M. High-Molecular-Weight Esters in α-Pinene Ozonolysis Secondary Organic Aerosol: Structural Characterization and Mechanistic Proposal for Their Formation from Highly Oxygenated Molecules. *Atmospheric Chem. Phys.* **2018**, *18* (11), 8453–8467. https://doi.org/10.5194/acp-18-8453-2018.
- Bateman, A. P.; Laskin, J.; Laskin, A.; Nizkorodov, S. A. Applications of High-Resolution Electrospray Ionization Mass Spectrometry to Measurements of Average Oxygen to Carbon Ratios in Secondary Organic Aerosols. *Environ. Sci. Technol.* **2012**, *46* (15), 8315–8324. https://doi.org/10.1021/es3017254.
 - (34) Bateman, A. P.; Nizkorodov, S. A.; Laskin, J.; Laskin, A. Photolytic Processing of Secondary Organic Aerosols Dissolved in Cloud Droplets. *Phys. Chem. Chem. Phys.* **2011**, *13* (26), 12199–12212. https://doi.org/10.1039/C1CP20526A.
 - (35) Laskin, J.; Eckert, P. A.; Roach, P. J.; Heath, B. S.; Nizkorodov, S. A.; Laskin, A. Chemical Analysis of Complex Organic Mixtures Using Reactive Nanospray Desorption Electrospray Ionization Mass Spectrometry. *Anal. Chem.* **2012**, *84* (16), 7179–7187. https://doi.org/10.1021/ac301533z.
 - (36) Roach, P. J.; Laskin, J.; Laskin, A. Molecular Characterization of Organic Aerosols Using Nanospray-Desorption/Electrospray Ionization-Mass Spectrometry. *Anal. Chem.* **2010**, *82* (19), 7979–7986. https://doi.org/10.1021/ac101449p.

- (37) Roach, P. J.; Laskin, J.; Laskin, A. Nanospray Desorption Electrospray Ionization: An Ambient Method for Liquid-Extraction Surface Sampling in Mass Spectrometry. *Analyst* **2010**, *135* (9), 2233–2236. https://doi.org/10.1039/C0AN00312C.
- 1000 (38) Pospisilova, V.; Lopez-Hilfiker, F. D.; Bell, D. M.; El Haddad, I.; Mohr, C.; Huang, W.; Heikkinen, L.; Xiao, M.; Dommen, J.; Prevot, A. S. H.; Baltensperger, U.; Slowik, J. G. On the Fate of Oxygenated Organic Molecules in Atmospheric Aerosol Particles. *Sci. Adv.* 2020, 6 (11), eaax8922. https://doi.org/10.1126/sciadv.aax8922.
 - (39) Kourtchev, I.; Szeto, P.; O'Connor, I.; Popoola, O. A. M.; Maenhaut, W.; Wenger, J.; Kalberer, M. Comparison of Heated Electrospray Ionization and Nanoelectrospray Ionization Sources Coupled to Ultra-High-Resolution Mass Spectrometry for Analysis of Highly Complex Atmospheric Aerosol Samples. *Anal. Chem.* **2020**, *92* (12), 8396–8403. https://doi.org/10.1021/acs.analchem.0c00971.
 - (40) Nizkorodov, S. A.; Laskin, J.; Laskin, A. Molecular Chemistry of Organic Aerosols through the Application of High Resolution Mass Spectrometry. *Phys. Chem. Chem. Phys.* **2011**, *13* (9), 3612–3629. https://doi.org/10.1039/C0CP02032J.
 - (41) Huang, Y.; Kenseth, C. M.; Dalleska, N. F.; Seinfeld, J. H. Coupling Filter-Based Thermal Desorption Chemical Ionization Mass Spectrometry with Liquid Chromatography/Electrospray Ionization Mass Spectrometry for Molecular Analysis of Secondary Organic Aerosol. *Environ. Sci. Technol.* **2020**, *54* (20), 13238–13248. https://doi.org/10.1021/acs.est.0c01779.
 - (42) Gao, S.; Keywood, M.; Ng, N. L.; Surratt, J.; Varutbangkul, V.; Bahreini, R.; Flagan, R. C.; Seinfeld, J. H. Low-Molecular-Weight and Oligomeric Components in Secondary Organic Aerosol from the Ozonolysis of Cycloalkenes and α-Pinene. *J. Phys. Chem. A* 2004, 108 (46), 10147–10164. https://doi.org/10.1021/jp047466e.
 - (43) Glasius, M.; Duane, M.; Larsen, B. R. Determination of Polar Terpene Oxidation Products in Aerosols by Liquid Chromatography–Ion Trap Mass Spectrometry. *J. Chromatogr. A* **1999**, *833* (2), 121–135. https://doi.org/10.1016/S0021-9673(98)01042-5.
 - (44) Cui, T.; Zeng, Z.; Santos, E. O. dos; Zhang, Z.; Chen, Y.; Zhang, Y.; Rose, C. A.; Budisulistiorini, S. H.; Collins, L. B.; Bodnar, W. M.; Souza, R. A. F. de; Martin, S. T.; Machado, C. M. D.; Turpin, B. J.; Gold, A.; Ault, A. P.; Surratt, J. D. Development of a Hydrophilic Interaction Liquid Chromatography (HILIC) Method for the Chemical Characterization of Water-Soluble Isoprene Epoxydiol (IEPOX)-Derived Secondary Organic Aerosol. *Environ. Sci. Process. Impacts* 2018, 20 (11), 1524–1536. https://doi.org/10.1039/C8EM00308D.
 - (45) Lin, Y.-H.; Budisulistiorini, S. H.; Chu, K.; Siejack, R. A.; Zhang, H.; Riva, M.; Zhang, Z.; Gold, A.; Kautzman, K. E.; Surratt, J. D. Light-Absorbing Oligomer Formation in Secondary Organic Aerosol from Reactive Uptake of Isoprene Epoxydiols. *Environ. Sci. Technol.* **2014**, *48* (20), 12012–12021. https://doi.org/10.1021/es503142b.
 - (46) Claeys, M.; Iinuma, Y.; Szmigielski, R.; Surratt, J. D.; Blockhuys, F.; Van Alsenoy, C.; Böge, O.; Sierau, B.; Gómez-González, Y.; Vermeylen, R.; Van der Veken, P.; Shahgholi, M.; Chan, A. W. H.; Herrmann, H.; Seinfeld, J. H.; Maenhaut, W. Terpenylic Acid and Related Compounds from the Oxidation of α-Pinene: Implications for New Particle Formation and Growth above Forests. *Environ. Sci. Technol.* 2009, 43 (18), 6976–6982. https://doi.org/10.1021/es9007596.
 - (47) West, C. P.; Hettiyadura, A. P. S.; Darmody, A.; Mahamuni, G.; Davis, J.; Novosselov, I.; Laskin, A. Molecular Composition and the Optical Properties of Brown Carbon Generated by the Ethane Flame. *ACS Earth Space Chem.* **2020**, *4* (7), 1090–1103. https://doi.org/10.1021/acsearthspacechem.0c00095.
 - (48) Hettiyadura, A. P. S.; Garcia, V.; Li, C.; West, C. P.; Tomlin, J.; He, Q.; Rudich, Y.; Laskin, A. Chemical Composition and Molecular-Specific Optical Properties of Atmospheric Brown Carbon Associated with Biomass Burning. *Environ. Sci. Technol.* **2021**, *55* (4), 2511–2521. https://doi.org/10.1021/acs.est.0c05883.
- 1045 (49) O'Brien, R. E.; Nguyen, T. B.; Laskin, A.; Laskin, J.; Hayes, P. L.; Liu, S.; Jimenez, J. L.; Russell, L. M.; Nizkorodov, S. A.; Goldstein, A. H. Probing Molecular Associations of Field-Collected and

- Laboratory-Generated SOA with Nano-DESI High-Resolution Mass Spectrometry. *J. Geophys. Res. Atmospheres* **2013**, *118* (2), 1042–1051. https://doi.org/10.1002/jgrd.50119.
- (50) Ebben, C. J.; Strick, B. F.; Upshur, M. A.; Chase, H. M.; Achtyl, J. L.; Thomson, R. J.; Geiger, F. M. Towards the Identification of Molecular Constituents Associated with the Surfaces of Isoprene-Derived Secondary Organic Aerosol (SOA) Particles. *Atmospheric Chem. Phys.* 2014, 14 (5), 2303–2314. https://doi.org/10.5194/acp-14-2303-2014.
- (51) Kitanovski, Z.; Grgić, I.; Veber, M. Characterization of Carboxylic Acids in Atmospheric Aerosols Using Hydrophilic Interaction Liquid Chromatography Tandem Mass Spectrometry. *J. Chromatogr. A* **2011**, *1218* (28), 4417–4425. https://doi.org/10.1016/j.chroma.2011.05.020.
- (52) Kitanovski, Z.; Grgić, I.; Vermeylen, R.; Claeys, M.; Maenhaut, W. Liquid Chromatography Tandem Mass Spectrometry Method for Characterization of Monoaromatic Nitro-Compounds in Atmospheric Particulate Matter. *J. Chromatogr. A* **2012**, *1268*, 35–43. https://doi.org/10.1016/j.chroma.2012.10.021.
- 1060 (53) Zhou, Y.; West, C. P.; Hettiyadura, A. P. S.; Pu, W.; Shi, T.; Niu, X.; Wen, H.; Cui, J.; Wang, X.; Laskin, A. Molecular Characterization of Water-Soluble Brown Carbon Chromophores in Snowpack from Northern Xinjiang, China. *Environ. Sci. Technol.* 2022, 56 (7), 4173–4186. https://doi.org/10.1021/acs.est.1c07972.
 - (54) Zhou, Y.; West, C. P.; Hettiyadura, A. P. S.; Niu, X.; Wen, H.; Cui, J.; Shi, T.; Pu, W.; Wang, X.; Laskin, A. Measurement Report: Molecular Composition, Optical Properties, and Radiative Effects of Water-Soluble Organic Carbon in Snowpack Samples from Northern Xinjiang, China. *Atmospheric Chem. Phys.* 2021, 21 (11), 8531–8555. https://doi.org/10.5194/acp-21-8531-2021.
 - (55) Reinnig, M.-C.; Müller, L.; Warnke, J.; Hoffmann, T. Characterization of Selected Organic Compound Classes in Secondary Organic Aerosol from Biogenic VOCs by HPLC/MSn. *Anal. Bioanal. Chem.* **2008**, *391* (1), 171–182. https://doi.org/10.1007/s00216-008-1964-5.
 - (56) Witkowski, B.; Gierczak, T. Characterization of the Limonene Oxidation Products with Liquid Chromatography Coupled to the Tandem Mass Spectrometry. *Atmos. Environ.* **2017**, *154*, 297–307. https://doi.org/10.1016/j.atmosenv.2017.02.005.
 - (57) Krechmer, J. E.; Groessl, M.; Zhang, X.; Junninen, H.; Massoli, P.; Lambe, A. T.; Kimmel, J. R.; Cubison, M. J.; Graf, S.; Lin, Y.-H.; Budisulistiorini, S. H.; Zhang, H.; Surratt, J. D.; Knochenmuss, R.; Jayne, J. T.; Worsnop, D. R.; Jimenez, J.-L.; Canagaratna, M. R. Ion Mobility Spectrometry–Mass Spectrometry (IMS–MS) for on- and Offline Analysis of Atmospheric Gas and Aerosol Species. *Atmospheric Meas. Tech.* 2016, 9 (7), 3245–3262. https://doi.org/10.5194/amt-9-3245-2016.
- 1080 (58) May, J. C.; Knochenmuss, R.; Fjeldsted, J. C.; McLean, J. A. Resolution of Isomeric Mixtures in Ion Mobility Using a Combined Demultiplexing and Peak Deconvolution Technique. *Anal. Chem.* **2020**, *92* (14), 9482–9492. https://doi.org/10.1021/acs.analchem.9b05718.
 - (59) May, J. C.; Goodwin, C. R.; Lareau, N. M.; Leaptrot, K. L.; Morris, C. B.; Kurulugama, R. T.; Mordehai, A.; Klein, C.; Barry, W.; Darland, E.; Overney, G.; Imatani, K.; Stafford, G. C.; Fjeldsted, J. C.; McLean, J. A. Conformational Ordering of Biomolecules in the Gas Phase: Nitrogen Collision Cross Sections Measured on a Prototype High Resolution Drift Tube Ion Mobility-Mass Spectrometer. *Anal. Chem.* **2014**, *86* (4), 2107–2116. https://doi.org/10.1021/ac4038448.
 - (60) Marchand, A.; Livet, S.; Rosu, F.; Gabelica, V. Drift Tube Ion Mobility: How to Reconstruct Collision Cross Section Distributions from Arrival Time Distributions? *Anal. Chem.* **2017**, *89* (23), 12674–12681. https://doi.org/10.1021/acs.analchem.7b01736.
 - (61) Viehland, L. A.; Mason, E. A. Gaseous Lon Mobility in Electric Fields of Arbitrary Strength. *Ann. Phys.* **1975**, *91* (2), 499–533. https://doi.org/10.1016/0003-4916(75)90233-X.
 - (62) Mason, E. A.; Schamp, H. W. Mobility of Gaseous Lons in Weak Electric Fields. *Ann. Phys.* **1958**, 4 (3), 233–270. https://doi.org/10.1016/0003-4916(58)90049-6.
- 1095 (63) Dodds, J. N.; Baker, E. S. Ion Mobility Spectrometry: Fundamental Concepts, Instrumentation, Applications, and the Road Ahead. *J. Am. Soc. Mass Spectrom.* **2019**, *30* (11), 2185–2195. https://doi.org/10.1007/s13361-019-02288-2.

- (64) Ibrahim, Y. M.; Garimella, S. V. B.; Prost, S. A.; Wojcik, R.; Norheim, R. V.; Baker, E. S.; Rusyn, I.; Smith, R. D. Development of an Ion Mobility Spectrometry-Orbitrap Mass Spectrometer Platform. Anal. Chem. 2016, 88 (24), 12152–12160. https://doi.org/10.1021/acs.analchem.6b03027.
- (65) Revercomb, H. E.; Mason, E. A. Theory of Plasma Chromatography/Gaseous Electrophoresis. Review. *Anal. Chem.* **1975**, *47* (7), 970–983. https://doi.org/10.1021/ac60357a043.
- (66) Butler, K. E.; Takinami, Y.; Rainczuk, A.; Baker, E. S.; Roberts, B. R. Utilizing Ion Mobility-Mass Spectrometry to Investigate the Unfolding Pathway of Cu/Zn Superoxide Dismutase. *Front. Chem.* **2021**, *9*.
- (67) Hopper, J. T. S.; Oldham, N. J. Collision Induced Unfolding of Protein Ions in the Gas Phase Studied by Ion Mobility-Mass Spectrometry: The Effect of Ligand Binding on Conformational Stability. J. Am. Soc. Mass Spectrom. 2009, 20 (10), 1851–1858. https://doi.org/10.1016/j.jasms.2009.06.010.
- (68) Lanucara, F.; Holman, S. W.; Gray, C. J.; Eyers, C. E. The Power of Ion Mobility-Mass Spectrometry for Structural Characterization and the Study of Conformational Dynamics. *Nat. Chem.* **2014**, *6* (4), 281–294. https://doi.org/10.1038/nchem.1889.
 - (69) Bohrer, B. C.; Merenbloom, S. I.; Koeniger, S. L.; Hilderbrand, A. E.; Clemmer, D. E. Biomolecule Analysis by Ion Mobility Spectrometry. *Annu. Rev. Anal. Chem.* **2008**, *I* (1), 293–327. https://doi.org/10.1146/annurev.anchem.1.031207.113001.
- 1115 (70) Jeanne Dit Fouque, K.; Fernandez-Lima, F. Following Structural Changes by Thermal Denaturation Using Trapped Ion Mobility Spectrometry–Mass Spectrometry. *J. Phys. Chem. B* **2020**, *124* (29), 6257–6265. https://doi.org/10.1021/acs.jpcb.0c04276.
 - (71) Ruotolo, B. T. Collision Cross Sections for Native Proteomics: Challenges and Opportunities. *J. Proteome Res.* **2022**, *21* (1), 2–8. https://doi.org/10.1021/acs.jproteome.1c00686.
- 1120 (72) Gadkari, V. V.; Ramírez, C. R.; Vallejo, D. D.; Kurulugama, R. T.; Fjeldsted, J. C.; Ruotolo, B. T. Enhanced Collision Induced Unfolding and Electron Capture Dissociation of Native-like Protein Ions. *Anal. Chem.* 2020, *92* (23), 15489–15496. https://doi.org/10.1021/acs.analchem.0c03372.
 - (73) Khristenko, N.; Amato, J.; Livet, S.; Pagano, B.; Randazzo, A.; Gabelica, V. Native Ion Mobility Mass Spectrometry: When Gas-Phase Ion Structures Depend on the Electrospray Charging Process. *J. Am. Soc. Mass Spectrom.* **2019**, *30* (6), 1069–1081. https://doi.org/10.1007/s13361-019-02152-3.
 - (74) Marchand, A.; Gabelica, V. Folding and Misfolding Pathways of G-Quadruplex DNA. *Nucleic Acids Res.* **2016**, *44* (22), 10999–11012. https://doi.org/10.1093/nar/gkw970.
 - (75) Iinuma, Y.; Ramasamy, S.; Sato, K.; Kołodziejczyk, A.; Szmigielski, R. Structural Characterisation of Dimeric Esters in α-Pinene Secondary Organic Aerosol Using N2 and CO2 Ion Mobility Mass Spectrometry. *Atmosphere* **2021**, *12* (1), 17. https://doi.org/10.3390/atmos12010017.
 - (76) Spolnik, G.; Wach, P.; Rudzinski, K. J.; Skotak, K.; Danikiewicz, W.; Szmigielski, R. Improved UHPLC-MS/MS Methods for Analysis of Isoprene-Derived Organosulfates. *Anal. Chem.* **2018**, *90* (5), 3416–3423. https://doi.org/10.1021/acs.analchem.7b05060.
 - (77) Hamlow, L. A.; Nei, Y. -w.; Wu, R. R.; Gao, J.; Steill, J. D.; Berden, G.; Oomens, J.; Rodgers, M. T. Impact of Sodium Cationization on Gas-Phase Conformations of DNA and RNA Cytidine Mononucleotides. *J. Am. Soc. Mass Spectrom.* **2019**, *30* (9), 1758–1767. https://doi.org/10.1007/s13361-019-02274-8.
 - (78) Poutsma, J. C.; Martens, J.; Oomens, J.; Maitre, P.; Steinmetz, V.; Bernier, M.; Jia, M.; Wysocki, V. Infrared Multiple-Photon Dissociation Action Spectroscopy of the B2+ Ion from PPG: Evidence of Third Residue Affecting B2+ Fragment Structure. *J. Am. Soc. Mass Spectrom.* **2017**, *28* (7), 1482–1488. https://doi.org/10.1007/s13361-017-1659-2.
 - (79) Vo, L.; Legaard, E.; Thrasher, C.; Jaffe, A.; Berden, G.; Martens, J.; Oomens, J.; O'Brien, R. E. UV/Vis and IRMPD Spectroscopic Analysis of the Absorption Properties of Methylglyoxal Brown Carbon. *ACS Earth Space Chem.* **2021**, *5* (4), 910–919. https://doi.org/10.1021/acsearthspacechem.1c00022.
 - (80) Walhout, E. Q.; Dorn, S. E.; Martens, J.; Berden, G.; Oomens, J.; Cheong, P. H.-Y.; Kroll, J. H.; O'Brien, R. E. Infrared Ion Spectroscopy of Environmental Organic Mixtures: Probing the

- Composition of α-Pinene Secondary Organic Aerosol. *Environ. Sci. Technol.* **2019**, *53* (13), 7604–7612. https://doi.org/10.1021/acs.est.9b02077.
- The state of the
- (82) Zhang, X.; Zhang, H.; Xu, W.; Wu, X.; Tyndall, G. S.; Orlando, J. J.; Jayne, J. T.; Worsnop, D. R.; Canagaratna, M. R. Molecular Characterization of Alkyl Nitrates in Atmospheric Aerosols by Ion Mobility Mass Spectrometry. *Atmospheric Meas. Tech.* **2019**, *12* (10), 5535–5545. https://doi.org/10.5194/amt-12-5535-2019.
 - (83) Zhang, X.; Krechmer, J. E.; Groessl, M.; Xu, W.; Graf, S.; Cubison, M.; Jayne, J. T.; Jimenez, J. L.; Worsnop, D. R.; Canagaratna, M. R. A Novel Framework for Molecular Characterization of Atmospherically Relevant Organic Compounds Based on Collision Cross Section and Mass-to-Charge Ratio. *Atmospheric Chem. Phys.* 2016, 16 (20), 12945–12959. https://doi.org/10.5194/acp-16-12945-2016.
 - (84) Skyttä, A.; Gao, J.; Cai, R.; Ehn, M.; Ahonen, L. R.; Kurten, T.; Wang, Z.; Rissanen, M. P.; Kangasluoma, J. Isomer-Resolved Mobility-Mass Analysis of α-Pinene Ozonolysis Products. *J. Phys. Chem. A* **2022**, *126* (30), 5040–5049. https://doi.org/10.1021/acs.jpca.2c03366.
 - (85) Zhao, Z.; Mayorga, R.; Lee, J.; Yang, X.; Tolentino, R.; Zhang, W.; Vuong, A.; Zhang, H. Site-Specific Mechanisms in OH-Initiated Organic Aerosol Heterogeneous Oxidation Revealed by Isomer-Resolved Molecular Characterization. ACS Earth Space Chem. 2020, 4 (5), 783–794. https://doi.org/10.1021/acsearthspacechem.0c00082.
- 1170 (86) Zhao, Z.; Tolentino, R.; Lee, J.; Vuong, A.; Yang, X.; Zhang, H. Interfacial Dimerization by Organic Radical Reactions during Heterogeneous Oxidative Aging of Oxygenated Organic Aerosols. *J. Phys. Chem. A* 2019, *123* (50), 10782–10792. https://doi.org/10.1021/acs.jpca.9b10779.
 - (87) Li, Z.; Valentine, S. J.; Clemmer, D. E. Complexation of Amino Compounds by 18C6 Improves Selectivity by IMS-IMS-MS: Application to Petroleum Characterization. *J. Am. Soc. Mass Spectrom.* **2011**, *22* (5), 817. https://doi.org/10.1007/s13361-011-0105-0.
 - (88) Reinecke, T.; Naylor, C. N.; Clowers, B. H. Ion Multiplexing: Maximizing Throughput and Signal to Noise Ratio for Ion Mobility Spectrometry. *TrAC Trends Anal. Chem.* **2019**, *116*, 340–345. https://doi.org/10.1016/j.trac.2019.03.014.
 - (89) Butler, K. E.; Dodds, J. N.; Flick, T.; Campuzano, I. D. G.; Baker, E. S. High-Resolution Demultiplexing (HRdm) Ion Mobility Spectrometry–Mass Spectrometry for Aspartic and Isoaspartic Acid Determination and Screening. *Anal. Chem.* **2022**, *94* (16), 6191–6199. https://doi.org/10.1021/acs.analchem.1c05533.
 - (90) Baboomian, V. J.; Gu, Y.; Nizkorodov, S. A. Photodegradation of Secondary Organic Aerosols by Long-Term Exposure to Solar Actinic Radiation. *ACS Earth Space Chem.* **2020**, *4* (7), 1078–1089. https://doi.org/10.1021/acsearthspacechem.0c00088.
 - (91) Bunce, N. J.; Schoch, J. P.; Zerner, M. C. Photorearrangement of Azoxybenzene to 2-Hydroxyazobenzene. Evidence for Electrophilic Substitution by Oxygen. *J. Am. Chem. Soc.* **1977**, 99 (24), 7986–7991. https://doi.org/10.1021/ja00466a034.
 - (92) Ligare, M. R.; Morrison, K. A.; Hewitt, M. A.; Reveles, J. U.; Govind, N.; Hernandez, H.; Baker, E. S.; Clowers, B. H.; Laskin, J.; Johnson, G. E. Ion Mobility Spectrometry Characterization of the Intermediate Hydrogen-Containing Gold Cluster Au7(PPh3)7H52+. *J. Phys. Chem. Lett.* **2021**, *12* (10), 2502–2508. https://doi.org/10.1021/acs.jpclett.0c03664.
 - (93) Stow, S. M.; Causon, T. J.; Zheng, X.; Kurulugama, R. T.; Mairinger, T.; May, J. C.; Rennie, E. E.; Baker, E. S.; Smith, R. D.; McLean, J. A.; Hann, S.; Fjeldsted, J. C. An Interlaboratory Evaluation of Drift Tube Ion Mobility–Mass Spectrometry Collision Cross Section Measurements. *Anal. Chem.* **2017**, *89* (17), 9048–9055. https://doi.org/10.1021/acs.analchem.7b01729.
 - (94) Roach, P. J.; Laskin, J.; Laskin, A. Higher-Order Mass Defect Analysis for Mass Spectra of Complex Organic Mixtures. *Anal. Chem.* **2011**, *83* (12), 4924–4929. https://doi.org/10.1021/ac200654j.

- (95) Kurulugama, R. T.; Darland, E.; Kuhlmann, F.; Stafford, G.; Fjeldsted, J. Evaluation of Drift Gas Selection in Complex Sample Analyses Using a High Performance Drift Tube Ion Mobility-QTOF Mass Spectrometer. *Analyst* **2015**, *140* (20), 6834–6844. https://doi.org/10.1039/C5AN00991J.
- (96) von Helden, G.; Hsu, M.; Kemper, P. R.; Bowers, M. T. Structures of Carbon Cluster Ions from 3 to 60 Atoms: Linears to Rings to Fullerenes. *J. Chem. Phys.* **1991**, *95* (5), 3835–3837. https://doi.org/10.1063/1.460783.
- 1205 (97) Prost, S. A.; Crowell, K. L.; Baker, E. S.; Ibrahim, Y. M.; Clowers, B. H.; Monroe, M. E.; Anderson, G. A.; Smith, R. D.; Payne, S. H. Detecting and Removing Data Artifacts in Hadamard Transform Ion Mobility-Mass Spectrometry Measurements. *J. Am. Soc. Mass Spectrom.* **2014**, *25* (12), 2020–2027. https://doi.org/10.1007/s13361-014-0895-y.
 - (98) Bilbao, A.; Gibbons, B. C.; Stow, S. M.; Kyle, J. E.; Bloodsworth, K. J.; Payne, S. H.; Smith, R. D.; Ibrahim, Y. M.; Baker, E. S.; Fjeldsted, J. C. A Preprocessing Tool for Enhanced Ion Mobility–Mass Spectrometry-Based Omics Workflows. *J. Proteome Res.* 2022, 21 (3), 798–807. https://doi.org/10.1021/acs.jproteome.1c00425.
 - (99) Gaussian 16, Revision C.01, Frisch, M. J.; Trucks, G. W.; Schlegel, H. B.; Scuseria, G. E.; Robb, M. A.; Cheeseman, J. R.; Scalmani, G.; Barone, V.; Petersson, G. A.; Nakatsuji, H.; Li, X.; Caricato, M.; Marenich, A. V.; Bloino, J.; Janesko, B. G.; Gomperts, R.; Mennucci, B.; Hratchian, H. P.; Ortiz, J. V.; Izmaylov, A. F.; Sonnenberg, J. L.; Williams-Young, D.; Ding, F.; Lipparini, F.; Egidi, F.; Goings, J.; Peng, B.; Petrone, A.; Henderson, T.; Ranasinghe, D.; Zakrzewski, V. G.; Gao, J.; Rega, N.; Zheng, G.; Liang, W.; Hada, M.; Ehara, M.; Toyota, K.; Fukuda, R.; Hasegawa, J.; Ishida, M.; Nakajima, T.; Honda, Y.; Kitao, O.; Nakai, H.; Vreven, T.; Throssell, K.; Montgomery, J. A., Jr.; Peralta, J. E.; Ogliaro, F.; Bearpark, M. J.; Heyd, J. J.; Brothers, E. N.; Kudin, K. N.; Staroverov, V. N.; Keith, T. A.; Kobayashi, R.; Normand, J.; Raghavachari, K.; Rendell, A. P.; Burant, J. C.; Iyengar, S. S.; Tomasi, J.; Cossi, M.; Millam, J. M.; Klene, M.; Adamo, C.; Cammi, R.; Ochterski, J. W.; Martin, R. L.; Morokuma, K.; Farkas, O.; Foresman, J. B.; Fox, D. J. Gaussian, Inc., Wallingford CT, 2016.
- 1225 (100) Shrivastav, V.; Nahin, M.; Hogan, C. J.; Larriba-Andaluz, C. Benchmark Comparison for a Multi-Processing Ion Mobility Calculator in the Free Molecular Regime. *J. Am. Soc. Mass Spectrom.* **2017**, 28 (8), 1540–1551. https://doi.org/10.1007/s13361-017-1661-8.
 - (101) Mesleh, M. F.; Hunter, J. M.; Shvartsburg, A. A.; Schatz, G. C.; Jarrold, M. F. Structural Information from Ion Mobility Measurements: Effects of the Long-Range Potential. *J. Phys. Chem.* **1996**, *100* (40), 16082–16086. https://doi.org/10.1021/jp961623v.
 - (102) Wu, T.; Derrick, J.; Nahin, M.; Chen, X.; Larriba-Andaluz, C. Optimization of Long Range Potential Interaction Parameters in Ion Mobility Spectrometry. *J. Chem. Phys.* **2018**, *148* (7), 074102. https://doi.org/10.1063/1.5016170.
 - (103) Campuzano, I.; Bush, M. F.; Robinson, C. V.; Beaumont, C.; Richardson, K.; Kim, H.; Kim, H. I. Structural Characterization of Drug-like Compounds by Ion Mobility Mass Spectrometry: Comparison of Theoretical and Experimentally Derived Nitrogen Collision Cross Sections. *Anal. Chem.* **2012**, *84* (2), 1026–1033. https://doi.org/10.1021/ac202625t.
 - (104) Zhang, Y.; Wang, K.; Tong, H.; Huang, R.-J.; Hoffmann, T. The Maximum Carbonyl Ratio (MCR) as a New Index for the Structural Classification of Secondary Organic Aerosol Components. *Rapid Commun. Mass Spectrom.* **2021**, *35* (14), e9113. https://doi.org/10.1002/rcm.9113.
 - (105) Morales, A. C.; Tomlin, J. M.; West, C. P.; Rivera-Adorno, F. A.; Peterson, B. N.; Sharpe, S. A. L.; Noh, Y.; Sendesi, S. M. T.; Boor, B. E.; Howarter, J. A.; Moffet, R. C.; China, S.; O'Callahan, B. T.; El-Khoury, P. Z.; Whelton, A. J.; Laskin, A. Atmospheric Emission of Nanoplastics from Sewer Pipe Repairs. *Nat. Nanotechnol.* 2022, *17* (11), 1171–1177. https://doi.org/10.1038/s41565-022-01219-9.
 - (106) Marsh, B. M.; Iyer, K.; Cooks, R. G. Reaction Acceleration in Electrospray Droplets: Size, Distance, and Surfactant Effects. *J. Am. Soc. Mass Spectrom.* **2019**, *30* (10), 2022–2030. https://doi.org/10.1007/s13361-019-02264-w.

- (107) Wei, Z.; Li, Y.; Cooks, R. G.; Yan, X. Accelerated Reaction Kinetics in Microdroplets: Overview and Recent Developments. *Annu. Rev. Phys. Chem.* **2020**, 71 (1), 31–51. https://doi.org/10.1146/annurev-physchem-121319-110654.
 - (108) Aiken, A. C.; DeCarlo, P. F.; Kroll, J. H.; Worsnop, D. R.; Huffman, J. A.; Docherty, K. S.; Ulbrich, I. M.; Mohr, C.; Kimmel, J. R.; Sueper, D.; Sun, Y.; Zhang, Q.; Trimborn, A.; Northway, M.; Ziemann, P. J.; Canagaratna, M. R.; Onasch, T. B.; Alfarra, M. R.; Prevot, A. S. H.; Dommen, J.; Duplissy, J.; Metzger, A.; Baltensperger, U.; Jimenez, J. L. O/C and OM/OC Ratios of Primary, Secondary, and Ambient Organic Aerosols with High-Resolution Time-of-Flight Aerosol Mass Spectrometry. *Environ. Sci. Technol.* 2008, 42 (12), 4478–4485. https://doi.org/10.1021/es703009q.
 - (109) Nguyen, T. B.; Roach, P. J.; Laskin, J.; Laskin, A.; Nizkorodov, S. A. Effect of Humidity on the Composition of Isoprene Photooxidation Secondary Organic Aerosol. *Atmospheric Chem. Phys.* **2011**, *11* (14), 6931–6944. https://doi.org/10.5194/acp-11-6931-2011.
 - (110) Lignell, H.; Epstein, S. A.; Marvin, M. R.; Shemesh, D.; Gerber, B.; Nizkorodov, S. Experimental and Theoretical Study of Aqueous Cis-Pinonic Acid Photolysis. *J. Phys. Chem. A* **2013**, *117* (48), 12930–12945. https://doi.org/10.1021/jp4093018.
 - (111) Gkatzelis, G. I.; Hohaus, T.; Tillmann, R.; Gensch, I.; Müller, M.; Eichler, P.; Xu, K.-M.; Schlag, P.; Schmitt, S. H.; Yu, Z.; Wegener, R.; Kaminski, M.; Holzinger, R.; Wisthaler, A.; Kiendler-Scharr, A. Gas-to-Particle Partitioning of Major Biogenic Oxidation Products: A Study on Freshly Formed and Aged Biogenic SOA. *Atmospheric Chem. Phys.* **2018**, *18* (17), 12969–12989. https://doi.org/10.5194/acp-18-12969-2018.
 - (112) Rister, A. L.; Martin, T. L.; Dodds, E. D. Application of Group I Metal Adduction to the Separation of Steroids by Traveling Wave Ion Mobility Spectrometry. *J. Am. Soc. Mass Spectrom.* **2019**, *30* (2), 248–255. https://doi.org/10.1007/s13361-018-2085-9.
 - (113) Kruve, A.; Kaupmees, K.; Liigand, J.; Oss, M.; Leito, I. Sodium Adduct Formation Efficiency in ESI Source. *J. Mass Spectrom.* **2013**, *48* (6), 695–702. https://doi.org/10.1002/jms.3218.
 - (114) Costalunga, R.; Tshepelevitsh, S.; Sepman, H.; Kull, M.; Kruve, A. Sodium Adduct Formation with Graph-Based Machine Learning Can Aid Structural Elucidation in Non-Targeted LC/ESI/HRMS. *Anal. Chim. Acta* **2022**, *1204*, 339402. https://doi.org/10.1016/j.aca.2021.339402.
 - (115) Bi, C.; Krechmer, J. E.; Frazier, G. O.; Xu, W.; Lambe, A. T.; Claflin, M. S.; Lerner, B. M.; Jayne, J. T.; Worsnop, D. R.; Canagaratna, M. R.; Isaacman-VanWertz, G. Coupling a Gas Chromatograph Simultaneously to a Flame Ionization Detector and Chemical Ionization Mass Spectrometer for Isomer-Resolved Measurements of Particle-Phase Organic Compounds. *Atmospheric Meas. Tech.* **2021**, *14* (5), 3895–3907. https://doi.org/10.5194/amt-14-3895-2021.
 - (116) Dodds, J. N.; May, J. C.; McLean, J. A. Correlating Resolving Power, Resolution, and Collision Cross Section: Unifying Cross-Platform Assessment of Separation Efficiency in Ion Mobility Spectrometry. *Anal. Chem.* **2017**, *89* (22), 12176–12184. https://doi.org/10.1021/acs.analchem.7b02827.
 - (117) Kundu, S.; Fisseha, R.; Putman, A. L.; Rahn, T. A.; Mazzoleni, L. R. High Molecular Weight SOA Formation during Limonene Ozonolysis: Insights from Ultrahigh-Resolution FT-ICR Mass Spectrometry Characterization. *Atmospheric Chem. Phys.* **2012**, *12* (12), 5523–5536. https://doi.org/10.5194/acp-12-5523-2012.
- 1290 (118) Jaoui, M.; Corse, E.; Kleindienst, T. E.; Offenberg, J. H.; Lewandowski, M.; Edney, E. O. Analysis of Secondary Organic Aerosol Compounds from the Photooxidation of D-Limonene in the Presence of NOX and Their Detection in Ambient PM2.5. *Environ. Sci. Technol.* **2006**, *40* (12), 3819–3828. https://doi.org/10.1021/es052566z.
 - (119) Chen, J.; Griffin, R. J. Modeling Secondary Organic Aerosol Formation from Oxidation of α-Pinene, β-Pinene, and d-Limonene. *Atmos. Environ.* **2005**, *39* (40), 7731–7744. https://doi.org/10.1016/j.atmosenv.2005.05.049.
 - (120) George, C.; Ammann, M.; D'Anna, B.; Donaldson, D. J.; Nizkorodov, S. A. Heterogeneous Photochemistry in the Atmosphere. *Chem. Rev.* **2015**, *115* (10), 4218–4258. https://doi.org/10.1021/cr500648z.

- 1300 (121) Baboomian, V. J.; Crescenzo, G. V.; Huang, Y.; Mahrt, F.; Shiraiwa, M.; Bertram, A. K.; Nizkorodov, S. A. Sunlight Can Convert Atmospheric Aerosols into a Glassy Solid State and Modify Their Environmental Impacts. *Proc. Natl. Acad. Sci.* **2022**, *119* (43), e2208121119. https://doi.org/10.1073/pnas.2208121119.
 - (122) Norrish, R. G. W.; Bamford, C. H. Photo-Decomposition of Aldehydes and Ketones. *Nature* **1937**, *140* (3535), 195–196. https://doi.org/10.1038/140195b0.
 - (123) Marchetti, B.; Karsili, T. N. V.; Ashfold, M. N. R. Exploring Norrish Type I and Type II Reactions: An Ab Initio Mechanistic Study Highlighting Singlet-State Mediated Chemistry. *Phys. Chem. Chem. Phys.* **2019**, *21* (26), 14418–14428. https://doi.org/10.1039/C8CP07292B.
 - (124) Morales, A. C.; Jayarathne, T.; Slade, J. H.; Laskin, A.; Shepson, P. B. The Production and Hydrolysis of Organic Nitrates from OH Radical Oxidation of β-Ocimene. *Atmospheric Chem. Phys.* **2021**, *21* (1), 129–145. https://doi.org/10.5194/acp-21-129-2021.
 - (125) Sarang, K.; Otto, T.; Rudzinski, K.; Schaefer, T.; Grgić, I.; Nestorowicz, K.; Herrmann, H.; Szmigielski, R. Reaction Kinetics of Green Leaf Volatiles with Sulfate, Hydroxyl, and Nitrate Radicals in Tropospheric Aqueous Phase. *Environ. Sci. Technol.* **2021**, *55* (20), 13666–13676. https://doi.org/10.1021/acs.est.1c03276.
 - (126) Fleming, L. T.; Ali, N. N.; Blair, S. L.; Roveretto, M.; George, C.; Nizkorodov, S. A. Formation of Light-Absorbing Organosulfates during Evaporation of Secondary Organic Material Extracts in the Presence of Sulfuric Acid. ACS Earth Space Chem. 2019, 3 (6), 947–957. https://doi.org/10.1021/acsearthspacechem.9b00036.
- 1320 (127) Sato, K.; Hatakeyama, S.; Imamura, T. Secondary Organic Aerosol Formation during the Photooxidation of Toluene: NOx Dependence of Chemical Composition. *J. Phys. Chem. A* **2007**, 111 (39), 9796–9808. https://doi.org/10.1021/jp071419f.
 - (128) Lin, P.; Liu, J.; Shilling, J. E.; Kathmann, S. M.; Laskin, J.; Laskin, A. Molecular Characterization of Brown Carbon (BrC) Chromophores in Secondary Organic Aerosol Generated from Photo-Oxidation of Toluene. *Phys. Chem. Chem. Phys.* **2015**, *17* (36), 23312–23325. https://doi.org/10.1039/C5CP02563J.
 - (129) West, C. P.; Morales, A. C.; Ryan, J.; Misovich, M. V.; Hettiyadura, A. P. S.; Rivera-Adorno, F.; Tomlin, J. M.; Darmody, A.; Linn, B. N.; Lin, P.; Laskin, A. Molecular Investigation of the Multi-Phase Photochemistry of Fe(III)–Citrate in Aqueous Solution. *Environ. Sci. Process. Impacts* **2022**. https://doi.org/10.1039/D1EM00503K.
 - (130) Beck, J.; Brüggemann, M.; van Pinxteren, D.; Herrmann, H. Nontarget Approach to Identify Complexing Agents in Atmospheric Aerosol and Rainwater Samples. *Anal. Chem.* **2022**, *94* (25), 8966–8974. https://doi.org/10.1021/acs.analchem.2c00815.
 - (131) Wojcik, R.; Webb, I. K.; Deng, L.; Garimella, S. V. B.; Prost, S. A.; Ibrahim, Y. M.; Baker, E. S.; Smith, R. D. Lipid and Glycolipid Isomer Analyses Using Ultra-High Resolution Ion Mobility Spectrometry Separations. *Int. J. Mol. Sci.* **2017**, *18* (1), 183. https://doi.org/10.3390/ijms18010183.
 - (132) Wojcik, R.; Nagy, G.; Attah, Isaac, K.; Webb, I. K.; Garimella, S. V. B.; Weitz, K. K.; Hollerbach, A.; Monroe, M. E.; Ligare, M. R.; Nielson, F. F.; Norheim, R. V.; Renslow, R. S.; Metz, T. O.; Ibrahim, Y. M.; Smith, R. D. SLIM Ultrahigh Resolution Ion Mobility Spectrometry Separations of Isotopologues and Isotopomers Reveal Mobility Shifts Due to Mass Distribution Changes. *Anal. Chem.* 2019, 91 (18), 11952–11962. https://doi.org/10.1021/acs.analchem.9b02808.
 - (133) Butler, K. E.; Baker, E. S. A High-Throughput Ion Mobility Spectrometry–Mass Spectrometry Screening Method for Opioid Profiling. *J. Am. Soc. Mass Spectrom.* **2022**, *33* (10), 1904–1913. https://doi.org/10.1021/jasms.2c00186.
- 1345 (134) DeRieux, W.-S. W.; Li, Y.; Lin, P.; Laskin, J.; Laskin, A.; Bertram, A. K.; Nizkorodov, S. A.; Shiraiwa, M. Predicting the Glass Transition Temperature and Viscosity of Secondary Organic Material Using Molecular Composition. *Atmospheric Chem. Phys.* **2018**, *18* (9), 6331–6351. https://doi.org/10.5194/acp-18-6331-2018.
 - (135) Rothfuss, N. E.; Petters, M. D. Influence of Functional Groups on the Viscosity of Organic Aerosol. *Environ. Sci. Technol.* **2017**, *51* (1), 271–279. https://doi.org/10.1021/acs.est.6b04478.

TOC

